Stony Brook University

The official electronic file of this thesis or dissertation is maintained by the University Libraries on behalf of The Graduate School at Stony Brook University.

SPH Simulations of Spiral Galaxy Interarm Structure

A Thesis Presented

by

Joern Wilhelm

to

The Graduate School

in Partial Fulfillment of the

Requirements

for the Degree of

Master of Arts

in

Physics

Stony Brook University

August 2010

Stony Brook University

The Graduate School

Joern Wilhelm

We, the thesis committee for the above candidate for the

Master of Arts degree, hereby recommend

acceptance of this thesis.

Assistant Professor, Ph.D., Jin Koda - Thesis Advisor
Department of Physics and Astronomy

Assistant Professor, Ph.D., Michael A. Zingale -
Chairperson of Defense
Department of Physics and Astronomy

Distinguished Teaching Professor, Ph.D., Harold J.
Metcalf -
Department of Physics and Astronomy

This thesis is accepted by the Graduate School

Lawrence Martin

Dean of the Graduate School

Abstract of the Thesis

SPH Simulations of Spiral Galaxy Interarm Structure

by
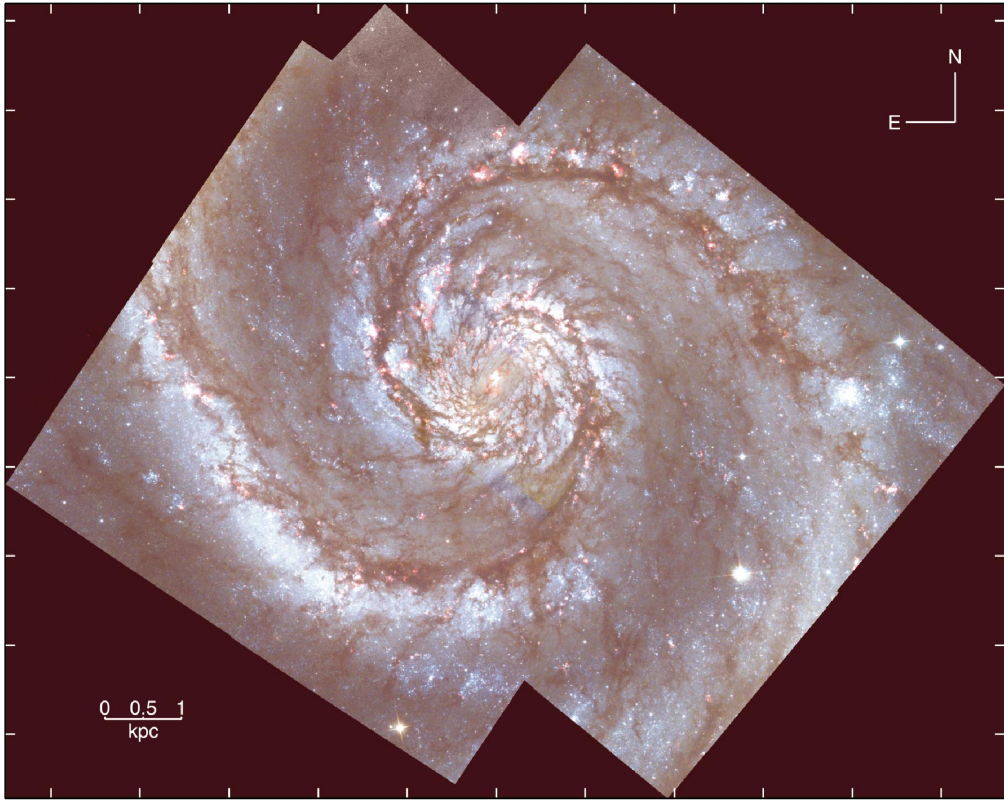
Joern Wilhelm

Master of Arts

in

Physics

Stony Brook University

2010

This work investigates the growth of substructures in spiral galaxies using Smoothed Particle Hydrodynamics(SPH) simulations. The impact of varying spiral arm potentials, gas temperatures and numerical resolutions onto interarm features, observed as feathering, is studied and compared to predictions made by the K-H instability model by Wada and Koda(2004) and the clump shearing model by Dobbs and Bonnell(2006). They are also compared to a recent Archival HST survey of Spiral Galaxy Feathering. The interarm features seen in SPH and relative pressure SPH(rpSPH) simulations, are found to be overall similar to observed feathers. High temperatures decreases velocity shear in the spiral arm shock regions and interarm structures are smoothed out entirely. Higher spiral arm potential strength increases velocity shear and the amount of interarm structures. While higher resolution is found to increase their visibility, the intrinsic interarm structures seem hardly affected. The effect of gas temperature and spiral arm potential strength variations onto gaseous interarm structure is found to be consistent with both theoretical models. An increase of interarm structure at low resolution as anticipated in the clump shearing model is not observed.

Hubble Space Telescope image of M51. (SC01)

Contents

List of Figures

Chapter 1

Introduction

Extinction features extending from galactic spiral arms to the interarm region were found for several grand design spiral galaxies as early as 1961 (Sandage 1961). They are not only impressive optical features, but are also possibly linked to and star formation. This raises the question, from which physical effect these structures originate? Due to the wide variety of interarm structure and complex physics of intergalactic gas, a comprehensive explanation has not yet been found.

This work investigates the growth of substructures in spiral arms using Smoothed Particle Hydrodynamics(SPH) simulations. It is based on the numerical method and parameters adopted in Wada and Koda(2004, hereafter WK04), where Kelvin-Helmholtz instabilities are suggested as a possible source for "wiggle instabilities"(WK04). To decide, whether a theoretical model relates to feathers observed in spiral galaxies, the substantiation of two links has to be tested; First, whether the wiggle instabilities can be assigned K-H instabilities or are caused by clump shearing as described by Dobbs and Bonnell(2006, hereafter DB06) or other theoretical models. Secondary, if wiggle instability seen in SPH simulations produces interarm features which resemble observations. The goal of this work is to clarify, whether parameter variations influence the interarm structure in SPH simulations as expected

by K-H Instabilities or as anticipated in the clump shearing model, which is also backed by SPH simulations. In addition to that, a brief comparison of simulations to recent Hubble Space Telescope(HST) observations is shown to ensure the relevance of structures seen in simulations for actual galaxies.

The necessary background information is provided in two introductory chapters. First it gives an overview over observational data on spiral galaxy substructure and feather characteristics. Then the three suggested theoretical models are introduced.

1.1 Observational Data of Spiral Arm Substructure

A brief summary of earlier observations focusing on intermediate sized structure in spiral galaxies is given, followed by a more detailed look at a recent high resolution HST survey.

1.1.1 Early Observations

Some of the first detailed notes on extinction features in galaxies were given by Sandage(1961) in the comments to The Hubble Atlas of Galaxies. He notices "principal dust lanes" at the inside edge of luminous spiral arms of Sc galaxies, but points out, that dust often is not confined to these lanes. Additional spiral shaped dust lanes can be found.

Weaver(1970), examining images of the Hubble Atlas, finds some galaxy arms "to be mottled and irregular, composed of clumps" and "frequently split and bifurcated". Furthermore he finds interarm features, "spurs" (also referred to "branches" or "twigs") originating "on the outside of [spiral] arms" and extending with a larger pitch angle. They can be seen as stellar features in the images. The inner part of the spiral arm shows a concentration of "dark material" that is "brushed out" over the outside edges.

628

Figure 1.1: Drawing of NGC 0628 sketching dust lanes and HII regions. (LY70)

At roughly the same time Lynds(1970, hereafter LY70) publishes a study on dark nebulae in 17 late type spirals, classified as Sc. Her study relies on 100- and 200-inch images taken with Mount Wilson and Palomar Observatories using photo plates sensitive in B-band and many others. Like Sandage, Lynds finds dark lanes along the inside of spiral arms, which she names "primary dust lanes "(PDLs)(LY70). In addition to the PDL along the spiral arms, she notices thinner dust lanes with $\sim 1/2$ the width of the PDLs "cutting" across bright arms with pitch angles of $\sim 50^o$ relative to the PDLs, which she refers to as "feathers". Finding most bright HII regions in her sample bordering or embedded in regions with high extinction, she assumes dust regions to be connected with star formation.

Piddington(1973) suggests a common origin of spurs and feathering based on joint appearances in galaxy images. Discussing whether the density wave theory proposed by Shu(1966) could provide a single explanation for both features, Elmegreen(1980) measured various properties of spurs in 7 late type spiral galaxies. Analyzing B-band and I-band images taken on the Palomar Schmidt telescope, Elmegreen finds 2-6 spurs per galaxy with an average

3

pitch angle of $63^o \pm 12^o$, which is close to the feather pitch angles found by LY70, supporting Piddington's claim. The spurs have lengths ranging from (1 - 5) kpc and an average width of (560 ± 260) pc, "typical of the widths of spiral arms"(LY70). She finds small groups of parallel spurs, but no spurs extending further than the next spiral arm.
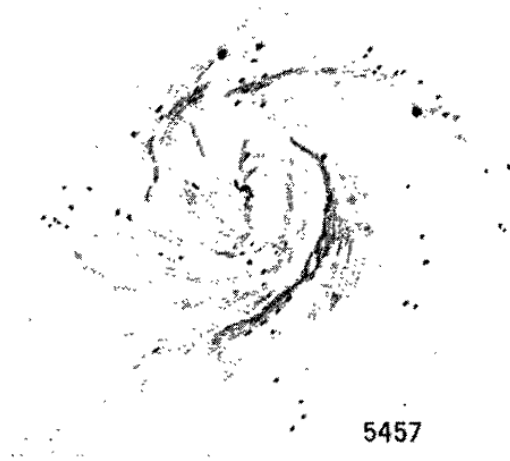
Figure 1.2: Drawing of NGC 5457 (M101) sketching dust lanes and HII regions. (LY70)

To prevent confusion, it is noted, that the terminology used in computational papers (Kim and Ostriker(2002, hereafter KO02); WK04; DB06) differs from terms used in observational papers as summarized by La Vigne et al.(2006, hereafter LV06):

- *Feathers* - Thin dust lanes or extinction features that extend outwards at a large angle from the PDL, which lines the inner side of the arm, cutting across the outer bright part of the spiral arm. (LY70)

- *Spurs* - Bright chains of OB associations and HII regions that jut at large angles from the spiral arm into the interarm regions. (Weaver 1970; Elmegreen 1980)

4

- *Branches* - Divarications of a spiral that lend to the overall spiral structure. (Elmegreen 1980)

This work adopts the term *spurs*, as it is applied in computational papers, where it is used to describe gas lanes of varying thickness extending outwards at a large angle from the PDL, often reaching the next spiral arm.

1.1.2 Feathers in HST, CO(1-0) and 8μm Images

The archival HST survey by La Vigne et al. greatly exceeds previous surveys (Elmegreen 1980; LY70) in sample size and resolution. With the analysis of over 200 galaxies using Hubble Space Telescope WFPC2 and Spitzer IRAC (3.6 - 8.0)μm images LV06 characterized the properties of feathers, e.g. feather delineation, frequency, spacing, shape and alliance with dense gas regions.

The survey is motivated by observational (Elmegreen 1980; Scoville 2001) and theoretical evidence (Balbus 1988, Kim and Ostriker 2002) to link feathers in spiral arms to star formation. Furthermore Vigne et al. assume feathers provide insight into important physical conditions of spiral galaxies, like gaseous surface density and magnetic fields.

General Characteristics of Feathers

LV06 describes feathers, as seen in fig: 1.3, as thin extinction features starting at the PDL at the inner part of spiral arms, crossing the luminous arm and sometimes extending into the interarm region. They find feathers are often parallel and have pitch angles and curvatures as described by LY70.

In galaxies where spurs and feathers were found, most spurs showed an overlaying feather. Because young and massive stars can be found in spurs, this connects feathers with spurs and star formation. Using feather positions from HST images La Vigne et al. found most feathers coincide with density peaks. Moreover, the feather spacing is found to increase with radius. The spacings of NGC 5194 are given in fig. 1.8. Measurements in NGC 3433 and
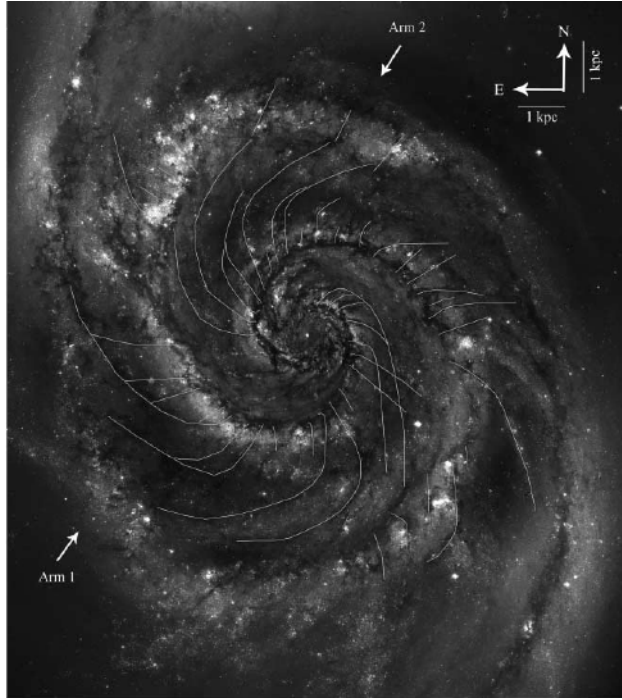
Figure 1.3: HST image of NGC 5194 (M51) with marked feathers. (LV06)

NGC 5985 show a similar increase in spacing.

In the survey, feathers are detected in 45 of 223 (20%) galaxies, where a detection is defined as a galaxy showing "multiple dust lanes with approximately regular spacing emerging from a PDL at roughly similar large angles, frequently associated with star formation"(LV06). Figure 1.4 shows the number of galaxies which carry feathers for each galaxy type.

LV06 uses the morphological classification theme for galaxies by de Vaucouler(1959). S stands for Spiral and describes galaxies with bright spiral arms. The letters a - d indicates a sequence from so-called early type to late type spirals. With increasing indices galaxies become less luminous, the pitch angle of spiral arms increases and the central bulge size shrinks relative to the disk.

While the detection rate is high for Sb (26%) and Sc (33%) galaxies, no feathers were found in dwarf spirals; Scd (0/36) and Sd (0/15). Very Few

6
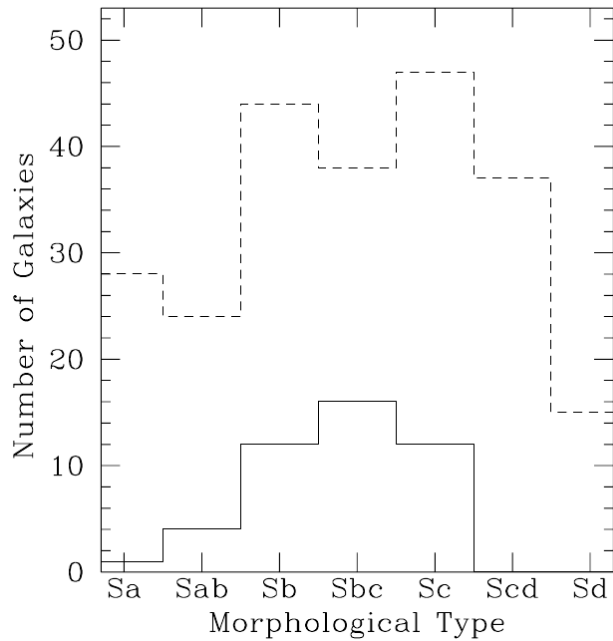
Figure 1.4: Distribution of galactic morphological types for the full sample (dashed line) and the ones that show feathers (solid line). (LV06)

feathers were found in early type galaxies; Sa (1/28) and Sb (4/24). Very few early types and none of the late types are found to show well defined PDLs. Thus, strong spiral arms tend to associate with feathers.

Analyzing fig. 1.4, LV06 supposes, that low gas abundance and low shock compression of the PDL due to shallower pitch angles are responsible for low detection rates for Sa-Sb types. For dwarf spirals LV06 accounts low density gradients between spiral arms and disk as well as generally low luminosities for the absence of feathering.

No difference in the numbers of feathers in barred and unbarred galaxies was found in the survey.

Feather Morphology

La Vigne gives a detailed analysis of the 45 galaxies associated with feathers listing characteristics mentioned in earlier surveys.

■ General Feather Shape - The pitch angle of feathers decreases after crossing the spiral arm due to shearing.

■ Beads on a string - 38 out of 45 galaxies show series of bright OB associations and HII regions along the PDL, lining feathers, in the spiral arm and as components of spurs, illustrated as "Beads on a string" by Elmegreen(1980).

■ Spurs - The survey finds spurs in 11 galaxies, all associated with feathers "transition[ing] to spurs across the outer edge of the spiral arm, forming a composite feature"(LV06).

■ Elongated Feathers - Feathers are described as "elongated" if they reach beyond the luminous arm into the interarm region. 29 out of 45 galaxies show elongated feathers. In 15 galaxies the longest ones connect to the PDL in the next arm. Furthermore elongated feathers show a decrease in pitch angle.

Feathers at 8μm and CO(1-0)

Because extinction features like feathers are hard to trace in areas with low background stellar density, it was not clear in earlier surveys to what extend feathers reach into the interarm region. La Vigne et al extend their survey using 8μm observations, thought to be emitted by Polycyclic Aromatic Hydrocarbons(PAHs) (Sellgren 1984), found in diffuse clouds. Overlaying the $8\mu m$ images with HST images, La Vigne et al. found that feathers stretch into the interarm region and can be traced with $8\mu m$ PAH emissions. To investigate molecular gas properties in spiral arms and feathers, velocity in-
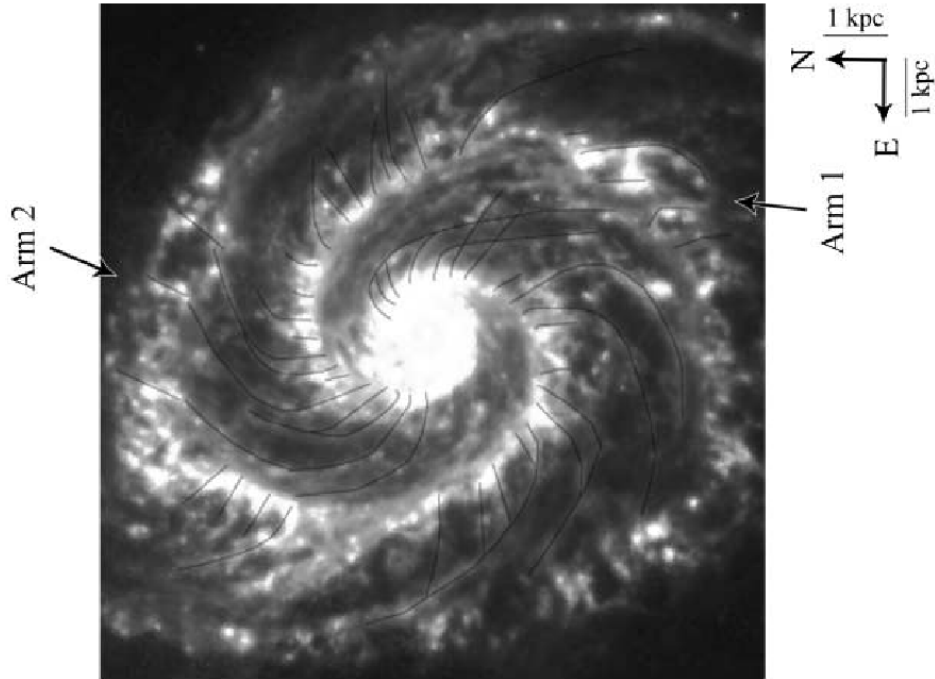
Figure 1.5: Spitzer 8μm image of NGC 5194 (M51) with marked feathers. (LV06)

tegrated CO(1-0) emission maps were used to trace high density regions. Interestingly, the survey found CO peaks located at the junction of feathers and the PDL they originate from "nearly"(LV06) 100 % of all feathers. In fewer cases higher CO brightness extending into the interarm regions along feathers was observed. La Vigne et al. conclude that the gas surface density is highest at the intersection and decreases by a factor of at least 5-10 with distance to the PDL.

The CO data could then be used to investigate feather spacing in a density plot along spiral arms for NGC 5194 and NGC 0628. To do this, they sample the CO map along the PDLs at the spiral arm. First they use a relation to calculate the H$_2$ column density N_{H_2} from CO emissions (Strong 1988),

$$N_{H_2} = 2.2 \times 10^{-20} (\frac{I_{CO}}{K km s^{-1}}) cm^{-2} \qquad (1.1)$$

9

Figure 1.6: BIMA SONG CO(1-0) image of NGC 5194 (M51) with marked feathers. (LV06)

then the molecular surface density Σ_{H_2} is calculated to be

$$\Sigma_{H_2} = 2.17 \times 10^{-20} N_{H_2} cos(i) M_\odot pc^{-2} \tag{1.2}$$

at each sampled point on the arm. The total gas surface density $\Sigma = \Sigma_{H_1} + \Sigma_{H_2} (M_\odot pc^{-2})$ is calculated by adding H_I data

$$\Sigma_{H_1} = 1.08 \times 10^{-20} N_{H_1} cos(i) M_\odot pc^{-2} \tag{1.3}$$

from Shostak and van der Kruit(1984).

Starting at the galactic center the H_2 surface density distribution seen in fig. 1.7 showed a density increase and peak at 1 kpc, which is approximately the galactocentric radius, followed by a steady decline with strong fluctuations. Figure 1.8 gives the feather spacing - distance dependency for both spiral arms of NGC 5194.

La Vigne concludes that the feather spacing increases with decreasing H_2 molecular gas density along spiral arms and therefore more feathers are found in denser, inner regions.

10
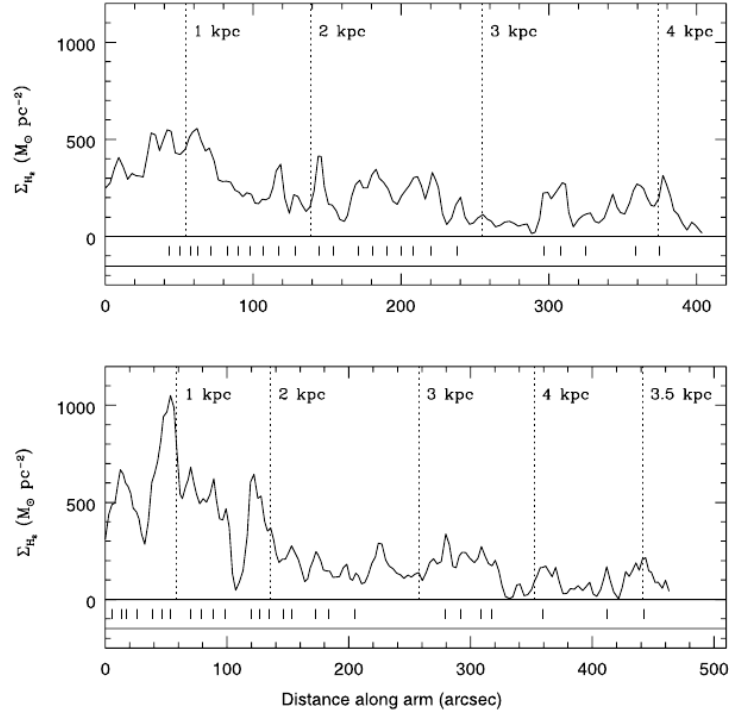
Figure 1.7: Total gas surface density along both spiral arms of NGC 5194. Showing a density decrease with distance to the galactic center and density peaks at feather-PDL connection points.(LV06)

1.2 Theoretical Studies of Spiral Arm Substructure

Several concepts try to explain spiral galaxy substructure like spurs, feathering and beads. In the following three models; the Kelvin-Helmholtz instability model(WK04), the clump instability model(DB06) and the magneto-Jeans instability(MJI)(KO02) are introduced. Our simulations do not include self-gravity nor magnetic fields which limits the comparability to simulations performed by Kim and Ostriker including these effects. Therefore the MJI model by Kim and Ostriker is beyond the scope of this work. However it is

11
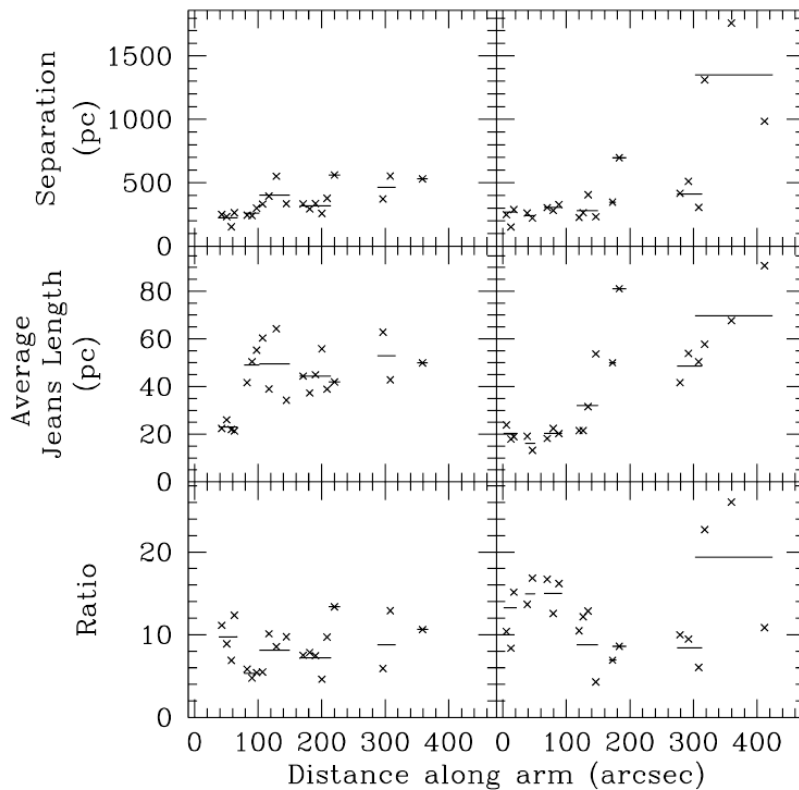
Figure 1.8: Feather spacing (top), local Jeans length (center) and ratio Jeans length/feather spacing (bottom) for NGC 5194. (LV06)

summarized to provide a complete overview.

1.2.1 Magneto-Jeans Instability

The theoretical basis for linear growth of self gravitating instabilities in spiral arms has been provided by Balbus(1988). His paper gives a general local dynamical stability analysis of a single fluid polytropic flow through the arms of spiral galaxies. The most important result of this paper was that linear perturbations have preferred directions of growth along and orthogonal to spiral arms. Balbus points out that this is a possible explanation for

observed extinction features like feathering, but also states, that his paper lacks falsifiable details and neglects likely important effects as magnetic fields and self-gravity. Furthermore, he suggests computer simulations to further investigate this problem.
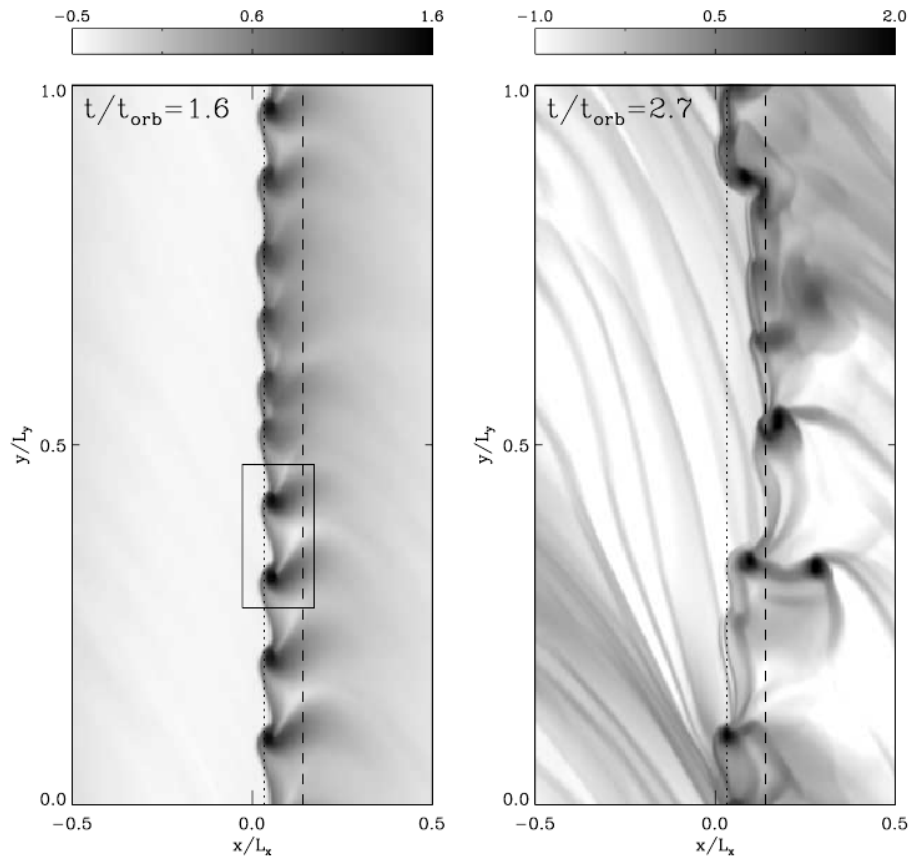
Figure 1.9: Logarithmic surface density plot showing a wiggle instability in simulations of a 2D disk excluding magnetic fields at two different stages of the simulation t/t_{orb}=1.6 (left) and t/t_{orb}=2.7 (right). (KO06)

In a series of three papers (2001 (KO01), 2002 (KO02),2006 (KO06)) Kim and Ostriker follow this call and perform Magneto-Hydro-Dynamic (MHD) simulations to understand the origin of intermediate scale structure in spiral galaxies. The simulations are carried out with a modified version of

13

Norman(1992) ZEUS code, which is a time explicit, operator split, finite difference method for solving the MHD equations on a mesh. While Kim and Ostriker(2001 and 2002) use a two dimensional disk, KO06 extends the simulations to three dimensions. With similar parameters to DB06 and WK04 (two armed spiral, pitch angle i = 10°, sound speed $c_0 = 7km/s$) Kim and Ostriker find regularly spaced feather-like features growing from spiral arms in magnetized disks. The magneto-Jeans instability is suggested as the responsible physical process for spur formation. The highly compressed gas in the shock regions of spiral arms starts to feel its own gravity. The internal gas pressure is not strong enough to prevent the gravitational collapse of gas clouds. This process is known as Jeans-Instability and the radius of a collapsing cloud is called Jeans-length. The gas clumps formed in this process get sheared and form feathers as the gas passes the spiral arm. KO02 found magnetic fields to reduce the growth time of dense clump by breaking the shear flow, which works against the gravitational instability.

Interestingly, Kim and Ostriker also find a wiggle instability in two dimensional, non-magnetic and weakly magnetic simulations, which they attribute to K-H instability. They do not find a wiggle instability in three dimensional simulations. Based on that they conclude, that it is an artifact of two dimensional models. But this view has recently been challenged by Wada(2008), who performed full three-dimensional hydrodynamic simulations including self-gravity, radiative cooling and star formation and found wiggle instabilities.

1.2.2 Feathering Caused by Sheared Pre Shock Structure

Dobbs and Bonnell(DB06) explain feathering with the shearing of dense gas of the interarm region as it crosses the shock that comes with passing spiral arms.
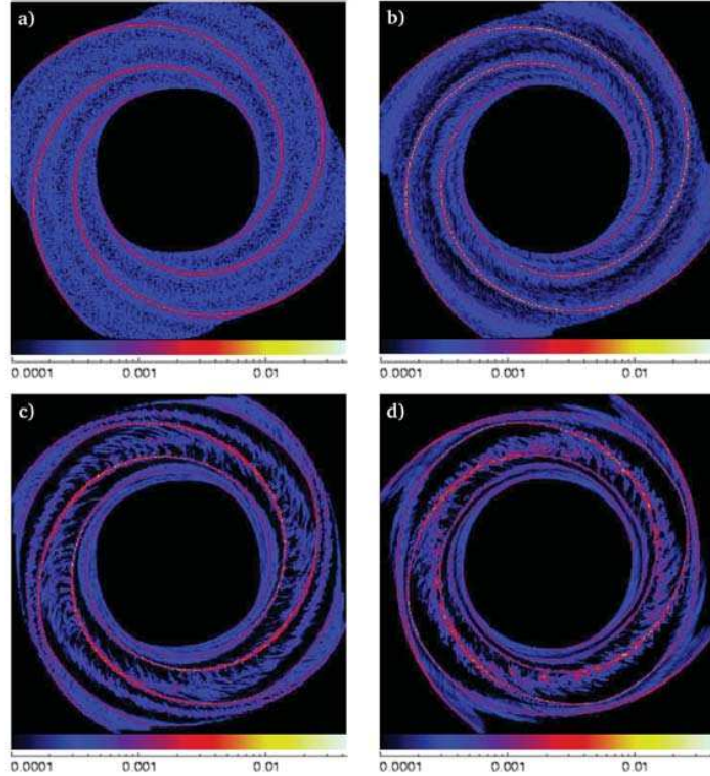
Figure 1.10: Column density plot of a 4x10^6 particle SPH spiral galaxy simulation assuming a gas temperature of T=50 K at different stages: a) 0 Myr b) 60 Myr c) 160 Myr d) 260 Myr. (DB06)

Simulation and Results

Dobbs and Bonnell use a SPH code based on Benz(1990), which is largely similar to the SPH code used in WK04. Heating and cooling, self-gravity, magnetic fields and stellar feedback are not included.

Figure 1.10 shows a snapshot of four different times in the highest resolution run using 4 x 10^6 particles with a temperature of 50 K. They identify the interarm structure as feathering. They point out that the structures seen in the interarm region in the later stage of the simulation (fig. 1.10 c) and d)) occur at the leading side of the spiral arm, while the trailing side is

15

smooth. Furthermore, they see a fairly regular feather spacing of ≈ 0.7 kpc evolving after 160 Myrs. DB06 observes a pitch angle decrease of spurs with increasing distance to the spiral arm.
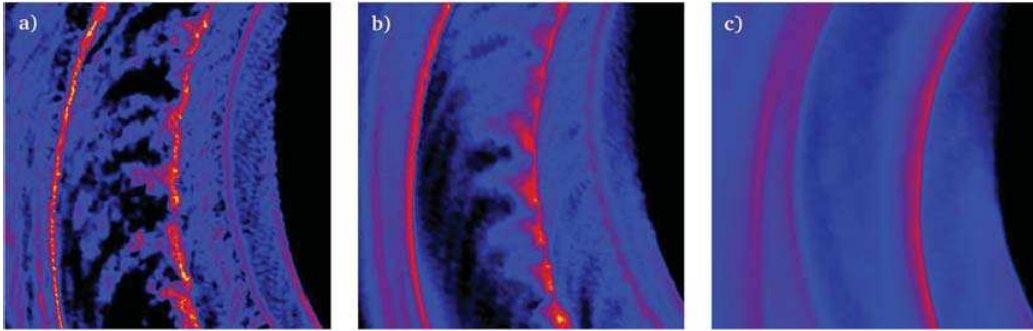
Figure 1.11: Column density plots for 10^6 particle SPH runs assuming a temperature of a) 100 K b) 1000 K c) 10^5 K. (DB06)

Higher temperature runs show an decrease in structure as seen in fig. 1.11. At a temperature of 10^4 K the interarm region is still smooth after 160 Myrs.

Interpretation

According to Dobbs and Bonnell spurs are formed by dense clumps sheared due to different orbits as the spiral arm passes by. They identify these clumps with Giant Molecular Clouds(GMCs) which are known to exist within spiral arms through observations. To prove this idea is consistent with their simulations, they mark a dense clump and follow the gas as it passes the shock. The evolution of this clump, seen in fig. 1.12, shows an evolved spur after 160 Myrs.

The dense clumps within the spiral arm are attributed to density inhomogenities in the inter arm region getting amplified by changes in angular momentum as they pass the spiral arm. The path and angular momentum of 5 particles is tracked in fig. 1.13. showing a harmonization between high
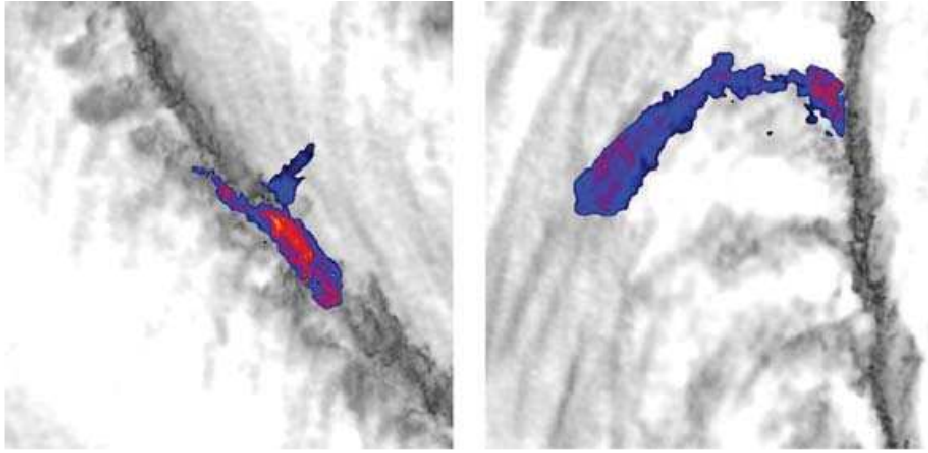
Figure 1.12: Plot showing a marked dense clump at 100 Myr (left) and the same clump sheared after 160 Myrs (right) in a T=50 K run. (DB06)
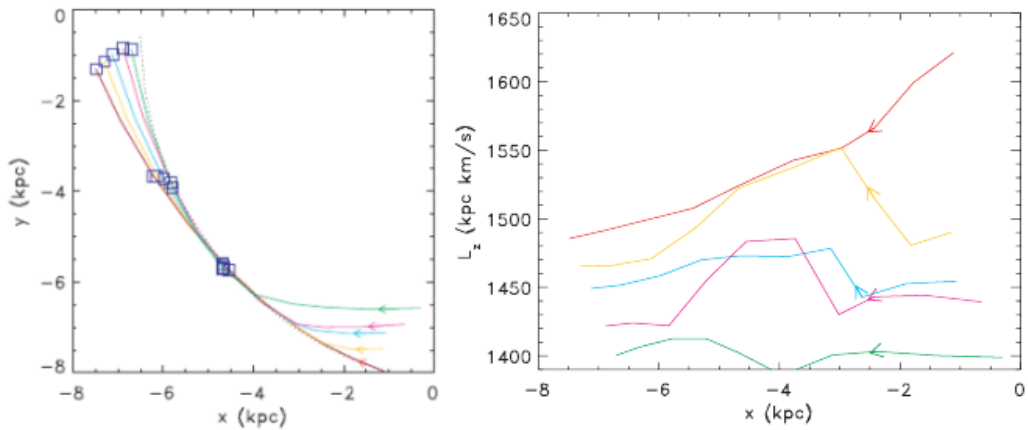
Figure 1.13: Left: Plot showing the orbits of 5 particles pre- and post-shock (marked with a dotted line). Right: Angular momentum of these particles as a function of distance to the galactic center. A harmonization of the particle angular momentum as these pass the spiral shock can be seen. (DB06)

angular momentum particles of outer orbits as they encounter lower angular momentum particles at inner orbits.

17

Dobbs et al. point out, that this model is consistent with the loss of structure at higher gas temperatures. A higher temperature leads to higher internal pressure, which smooths out interarm structure, so that there aren't any clumps left to get shared as the gas passes the shock region.

1.2.3 Kevin-Helmholtz Instability

Another origin for the characteristic extinction features of spiral galaxies is suggested by WK04. They claim, that spiral shocks in thin galactic disks are dynamically unstable and lead to hydrodynamic instability, presumably Kelvin-Helmholtz instability, occurring at high velocity gradients in gas shocked by the spiral density wave. They perform non-self-gravitating, non-magnetic hydrodynamic simulations of gas in spiral and barred potentials with three different codes.
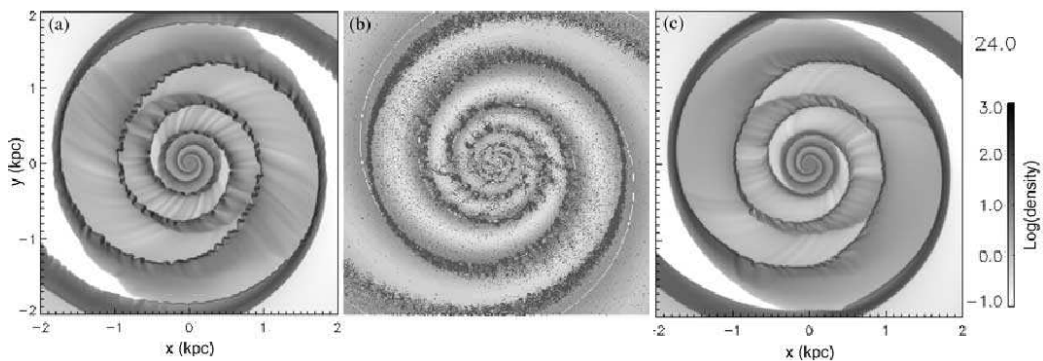
Figure 1.14: Snapshot of spiral galaxy gas simulations with three different numerical schemes: AUSM (left), SPH (center) and CIP (right) at a simulation time of t = 24 Myr. Despite the different codes all simulations show a wiggle and ripple structure. (WK04)

Simulation and Results

The three different codes applied are AUSM, SPH and CIP.

■ - AUSM (Advection Upstream Splitting Method) is an Euler-mesh code developed by Liou and Steffen(1993).

■ - CIP (Cubic Interpolated Propagation) is a mesh based semi-Lagrangian method developed by Yabe and Aoki(1991). For both codes, Cartesian grids with 128^2-2048^2 zones were used.

■ SPH (Smoothed Particle Hydrodynamics) is a mesh free Lagrangian code originally developed by Lucy(1977). Wada and Koda use a version of Benz(1990) SPH code which they modified. A closer examination of SPH is given in section 2.1.

The gas behaves similarly in all three simulations. The shock front is found to be unstable, showing structure they referred to as "ripples" or "wiggles"(WK04). The interarm region displays spurs emerging from wiggles in the shock front with a regular spacing of the order of ~ 100 pc.

Several different rotation curves were adopted as listed in fig. 1.15. Simulations using a flat rotation curve (model B) and standard parameters were free of ripples and wiggles and therefore shocks in models alike were considered to be stable.

Furthermore, they extended their simulations to smaller (5°) and wider (20°) galactic pitch angles than previously adopted. The pitch angle was found to have a strong impact on the stability of the spiral shock as discussed by Nelson and Matsuda(1977). While unstable at high pitch angles, tightly wound spirals don't show wiggles and ripples.
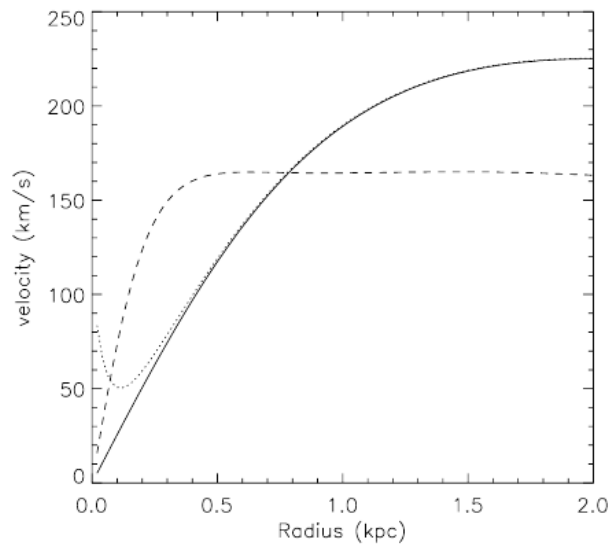
Figure 1.15: Different rotation curves used in WK04. Model A; rigid rotation (solid line), model B; flat rotation curve (dashed line) and model D; bar potential with central black hole (dotted line). (WK04)
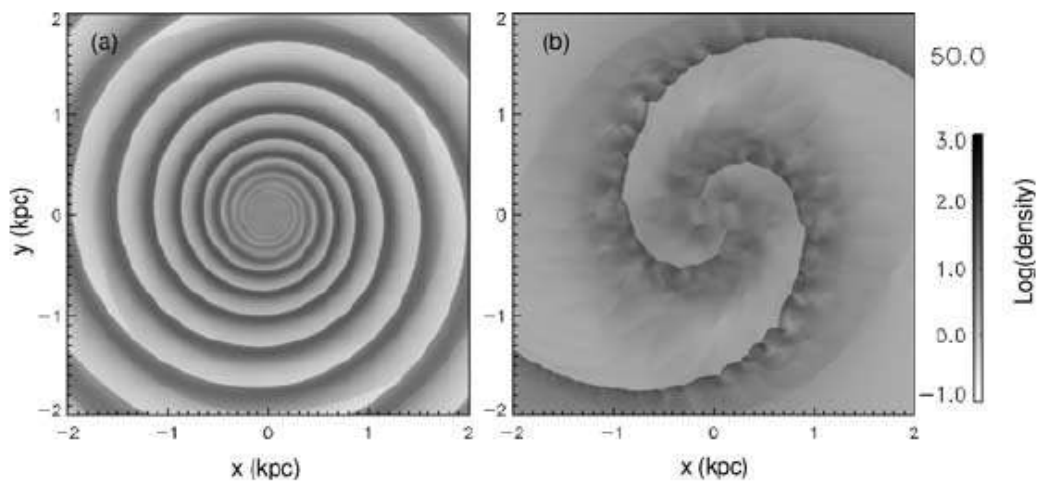
Figure 1.16: AUSM simulation with a rigid rotation curve using a pitch angle of 5° (left) and 20° (right). (WK04)

Interpretation

Wada and Koda suggest K-H instability as source for wiggle and ripple structure observed in the simulations. K-H instability occurs, if a high velocity shear is present in a continuous fluid or at the contact surface between two different fluids. The instability creates a dense region with an internal angular momentum gradient. Due to angular momentum conservation the gas with high angular momentum leaves the spiral arm into the interarm region, stretching the dense clump into a line. To support their claim, they calculate
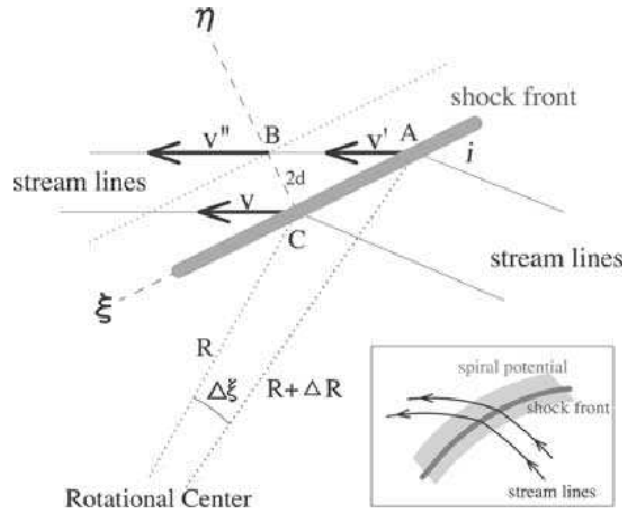
Figure 1.17: Schematic image of streamlines crossing the shock region at spiral arms. The simplification is made, that streamlines and shock are straight. (WK04)

the dimensionless Richardson number J, defined as

$$J := -\frac{g}{\rho}\frac{d\rho/dz}{(du/dz)^2} \tag{1.4}$$

where u is the shear velocity and g the gravitational acceleration perpendicular to the shock. The Richardson number gives the ratio between potential energy (buoyancy force) and kinetic energy (inertia). $J > 1/4$ is a necessary

21

but not sufficient condition for K-H stability.

Assuming isothermal flow and straight streamlines, Wada and Koda give an approximation of the Richardson criteria for a 2d thick gas layer behind the shock (see scheme)

$$J \approx \frac{2\epsilon d}{RSin(i)(1 - Sin^2(i))(1 - 1/M^2)^2} \tag{1.5}$$

where M is the Mach number. According to eq.(1.4) J increases with higher M and smaller pitch angles, resulting in higher K-H stability.

Chapter 2

Method

The basis of this work are simulations performed with the Smoothed Particle Hydrodynamics code. In the following the main ideas of SPH and details regarding the version adopted in this work are summarized.

For comparison I realized a new scheme of SPH called relative pressure SPH(rpSPH), which is found to alter the interarm gas structure only slightly. A detailed comparison is given in sec. 3.1. In the following the differences between SPH and rpSPH are outlined and the changes necessary to implement rpSPH are given. After that, further details regarding the spiral galaxy potential and other parameters of the simulations are reviewed.

2.1 SPH

SPH is a numerical finite element method to solve the hydrodynamic equations developed by Lucy(1977). It is a mesh-free, Lagrangian code widely used in astrophysics to simulate gas flow. The main idea is, that the motions of fluid elements can be followed by solving the equations of motion of particles which carry physical information. Field quantities like density, pressure, temperature, etc. are calculated by averages from these particles.

In particular, the mathematical core of SPH is that any field quantity

$A(\vec{r})$ can be represented as an integral over a delta function,

$$A(\vec{r}) = \int A(\vec{r'})\delta(\vec{r} - \vec{r'})d\vec{r'} \approx \int A(\vec{r'})W(\vec{r} - \vec{r'}, h)d\vec{r'} \tag{2.1}$$

which itself can be interpolated with an integral over a so-called Kernel function $W(\vec{r} - \vec{r'}, h)$ that satisfies

$$\int W(\vec{r} - \vec{r'}, h)d\vec{r'} = 1 \text{ and } \lim_{h \to 0} W(\vec{r} - \vec{r'}, h) = \delta(\vec{r} - \vec{r'}) \tag{2.2}$$

Physically, this means, that field quantities can be calculated from a infinite number of particles, that covers every point in the field. In simulations, one is limited to a finite set of particles. To gain the field quantities from that, the delta function needs to be approximated by a Kernel function that smooths over a limited set of particles in a certain area confined by the smoothing length h. For a finite number of particles the integration interpolant is

$$A(\vec{r}) = \sum_b m_b \frac{A_b}{\rho_b} W(\vec{r} - \vec{r}_b, h) \tag{2.3}$$

This sums over all particles b with the physical quantities, mass m_b, density ρ_b and position r_b . A_b can be the value of any quantity A of particle b at position r$_b$. This has the advantage, that operators applied to the interpolant only effect the Kernel function. While a Gauss-kernel $W(x, h) = \frac{1}{h\sqrt{\pi}}e^{-(x/h^2)}$ is a natural choice to fulfill (2.2), for computational reasons many codes prefer certain piecewise polynomials, so-called splines. Splines have the advantage, that they cut off the tails of the Gauss function limiting the amount of particles smoothed over.

Conceptually, the area (2D) or volume (3D) constrained by the smoothing length gives the size of a SPH particle, because it describes the area the Kernel function recognizes the environment. Using a Gauss function, every particle would have the size of the simulation and be influenced (although minimally) by conditions far away from the box position that needs to be calculated. Hydrodynamic forces are by nature short ranged forces and therefore there is no need to include far away particles. This reduces the amount of particle-particle interactions significantly. Furthermore values of splines

or other kernels can be pre calculated and drawn from a table to speed up the simulation.

The WK04 SPH code used for the simulations in this work implements a spline kernel

$$W(\vec{r}, h) = \frac{10}{7\pi h^2} \begin{cases} 1 - \frac{3}{2}q^2 + \frac{3}{4}q^3 & \text{if } 0 \le \frac{r}{h} \le 1; \\ \frac{1}{4}(2 - q)^3 & \text{if } 1 \le \frac{r}{h} \le 2; \\ 0 & \text{if otherwise ;} \end{cases} \tag{2.4}$$

by Monaghan(1992).

To increase the resolution in areas with high density and lower the resolution in areas with low density, the smoothing length and therefore the size of an SPH particle is allowed to vary with space and time.

$$h_{i+1} = h_i \times \frac{1}{2}[1 + (\frac{N_{av}}{N_{neighbor}})^{1/2}] \tag{2.5}$$

As described in equation (2.5) the smoothing length of the next time step is adjusted in a way that the number of neighbor particles $N_{neighbor}$ is kept close to a fixed average particle number N_{av}. N_{av} is set to 32 for all simulations performed.

To calculate the fluid flow one has to implement and solve the Navier-Stokes-equation using the mass and energy conservation laws. The acceleration gained from that is then used to move the Lagrangian particles in the way, that they follow the gas flow. The gas in the simulations performed in this work is isothermal. Therefore the energy is not conserved, when the gas faces rapid compressions. The SPH code used in (WK04) and this work implements the continuity equation

$$\frac{\partial \Sigma_g}{\partial t} + \nabla(\Sigma_g v) = 0 \tag{2.6}$$

and Navier Stokes Equation,

$$\frac{\partial v}{\partial t} + (v\nabla)v + \frac{\nabla p}{\Sigma_g} = -\nabla \Phi_{ext} \tag{2.7}$$

in two dimensions . Σ_g is the surface density, v the velocity Φ_{ext} an external potential and p the pressure. With the use of equation (2.3), eq. (2.6) and (2.7) can be implemented into SPH

$$\frac{d\rho_a}{dt} = \sum_b m_b \boldsymbol{v}_{ab} \nabla_a W_{ab} \tag{2.8}$$

$$\frac{dv_a}{dt} = -\sum_b (m_b)(\frac{P_b}{\rho_b^2} + \frac{P_a}{\rho_a^2} + \Pi_{ab}) \nabla_a W_{ab} \tag{2.9}$$

where $\boldsymbol{v}_{ab} = \boldsymbol{v}_a - \boldsymbol{v}_b$ and $W_{ab} = W(\boldsymbol{r}_a - \boldsymbol{r}_b, h)$. This representation following Monoghan(1992) addresses the problem, that gradient terms, if not written in a symmetrized way, are not symmetric to particle exchange and therefore violate conservation laws. If one does not symmetrize the pressure gradient term and rewrites it in this way

$$\frac{\nabla P}{\rho} = \nabla(\frac{P}{\rho}) + \frac{P}{\rho^2} \nabla \rho \tag{2.10}$$

one will get a momentum equation, where the force of particle a on b is not equal and opposite to the force of particle b on a, because of different pressure values P_a and P_b. This is seen fig. 2.11 taking into account that $\nabla_a W_{ab} = -\nabla_b W_{ab}$.

$$\frac{m_a m_b P_b}{\rho_a \rho_b} \nabla_a W_{ab} \neq -\frac{m_a m_b P_a}{\rho_a \rho_b} \nabla_b W_{ab} \tag{2.11}$$

Rewriting formulae with the density placed inside operators is necessary in several equations of SPH.

Adding a term Π_{ab} to the momentum equation (2.9) is one way to include artificial viscosity. Π_{ab} adopted for this work is

$$\Pi_{ab} = \begin{cases} \frac{\alpha \bar{c}_{ab} \mu_{ab} + \beta \mu_{ab}^2}{\bar{\rho}_{ab}} & \text{if } \boldsymbol{v}_{ab} \boldsymbol{r}_{ab} < 0; \\ 0 & \text{if } \boldsymbol{v}_{ab} \boldsymbol{r}_{ab} > 0; \end{cases} \tag{2.12}$$

with

$$\mu_{ab} = \frac{h \boldsymbol{v}_{ab} \boldsymbol{r}_{ab}}{\boldsymbol{r}_{ab} + \eta} \tag{2.13}$$

where $\boldsymbol{r}_{ab} = (\boldsymbol{r}_a - \boldsymbol{r}_b)$ is the spacing and $\boldsymbol{v}_{ab} = (\boldsymbol{v}_a - \boldsymbol{v}_b)$ the velocity difference. It contains a linear $\boldsymbol{v}_{ab}$ term for shear viscosity and a quadratic $\boldsymbol{v}_{ab}$ term to handle shocks. The other parameters are empirically constrained from shock tube test calculations to $\alpha \approx 1, \beta \approx 2$ and $\eta^2 = 0.01h^2$.

One way to move the particles is to adopt the definition of the velocity.

$$\frac{d\vec{r}}{dt} = \vec{v} \tag{2.14}$$

The numerical integration is commonly (Abel 2010; WK04; DB06) carried out with a leapfrog integrator. This method is similar to the standard Euler integrator, but approximately conserves energy.

2.2   rpSPH

The modifications necessary to gain a relative pressure version of SPH are given by Tom Abel in the very recent paper Abel(2010, hereafter TA10). rpSPH - standing for relative pressure SPH is motivated by shortcomings of SPH. Among other errors, most SPH variations don't reproduce Rayleigh-Taylor instabilities and have artificial surface tension and clumping.

Abel attributes the way the momentum equation in SPH is discretized for these errors. The basis for rpSPH in TA10 is the SPH code Gadget-2 by Springel and Hernquist(2002), which he modifies. The equation of motion used in Gadget-2 is

$$\frac{d\vec{v_i}}{dt} = -\sum_{j=1}^{N} m_j [f_i \frac{p_i}{\rho_i^2} \nabla_i W_{ij}(h_i) + f_j \frac{p_j}{\rho_j^2} \nabla_i W_{ij}(h_j)] \tag{2.15}$$

with f_i defined by

$$f_i = [1 + \frac{h_i}{3\rho_i} \frac{\partial \rho_i}{\partial h_i}]^{-1} \tag{2.16}$$

and $W_{ij}(h) = W(|\vec{r}_i - \vec{r}_j|, h)$ is a short form for a kernel function W allowing the smoothing length h to vary. As Monaghan pointed out early, particles, as soon as there is pressure, apply identical but opposing force on each other,

27

pushing them apart. That can be seen in eq. (2.9) where the pressure terms $\frac{P_a}{\rho_a^2}$ and $\frac{P_b}{\rho_b^2}$ are added. This symmetric form of the equation of motion ensures linear momentum conservation. But Abel argues, that for Lagrangian fluid elements, symbolizing a certain amount of fluid and not single gas particles, a force should only apply in case of a pressure gradient as described in the pressure gradient part of the Navier Stokes equation $\rho\frac{D\vec{v}}{Dt} = -\nabla p$. Assuming two fluid particles with the same pressure in SPH, these particles accelerate each other to infinity, while in rpSPH they stand still. To avoid an ever present force, TA10 subtracts the pressure of the interacting particles from the pressure of all particles, which changes eq. (2.15) to

$$\frac{d\vec{v_i}}{dt} = \sum_{j=1}^{N} m_j [f_i \frac{P_j - P_i}{\rho_j^2} \frac{1}{2} [\nabla_i W_{ij}(h_i) + \nabla_i W_{ij}(h_j)]]. \qquad (2.17)$$

This new equation of motion breaks the symmetry in force, which can be understood with the two particle example. In rpSPH two particles with a pressure gradient both move in the same direction as given by the gradient. The total force is not zero. Therefore the angular momentum conservation is not given anymore. Whether this has an significant effect on the simulations performed in this work is described in sec. 3.3.

Despite this shortcoming, Abel finds rpSPH to be superior to standard SPH in various tests. Especially related to the use of SPH/rpSPH in the simulation of gas in spiral galaxies is the ability of the code to prevent artificial clumping caused by velocity noise. Abel argues that rpSPH shows a strong decrease of velocity noise compared to SPH. Figure 2.1 shows the total kinetic energy of 50^2 particles initialized onto a regular grid with zero initial velocities in several rpSPH and SPH simulations. While the velocity noise in SPH seen in this configuration is non isotropic and leads to artificial clumping, rpSPH shows a velocity noise several orders of magnitude lower and is stated to be clump free.

The rpSPH code's ability to tackle K-H instability is tested in a setup solved analytically by Chandrasekhar(1961). It consists of two fluids with different densities and a velocity shear of $\Delta v = v_2 - v_1$ in a 1x1 box with
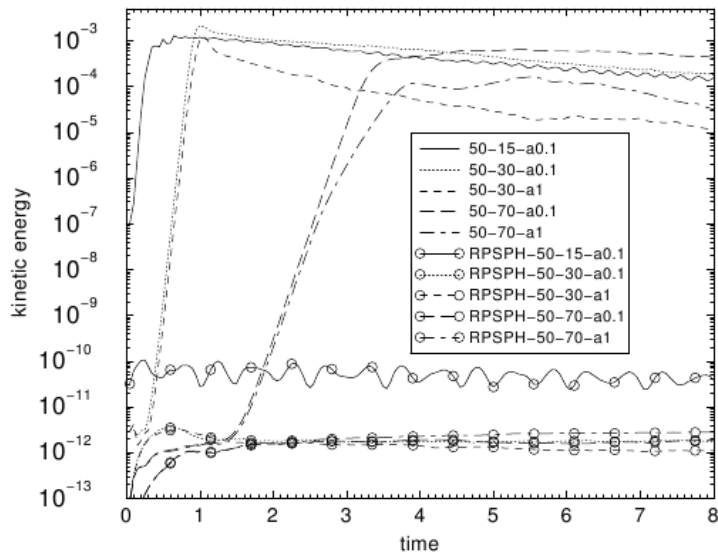
Figure 2.1: The plot shows the total kinetic energy as a function of time for various SPH and rpSPH simulations initializing the particles on a regular lattice and zero initial velocity. The table lists the parameters used: square root of the particle number - number of neighbors - artificial viscosity parameter alpha. (TA10)

continuous boundary conditions. The fluids are arranged in three layers with one fluid in between ($| v - 0.5 | < 0.25$) the other one ($| v - 0.5 | > 0.25$). Although the K-H instability is reproduced in the normal SPH version fairly well, see fig. 2.2, the comparison with rpSPH and the grid based Code *ENZO* yields less artificial ripples and a correct growth rate at smaller velocity perturbations in the new rpSPH version.

With less artificial clumping and a better modeling of K-H instabilities the usage of rpSPH in gas simulations should reduce the risk of misinterpreting numerical errors as physical features and comparison to SPH results enhances the visibility of these numerical errors.

The SPH version implemented in WK04 and this work (eq. 2.15) lacks the
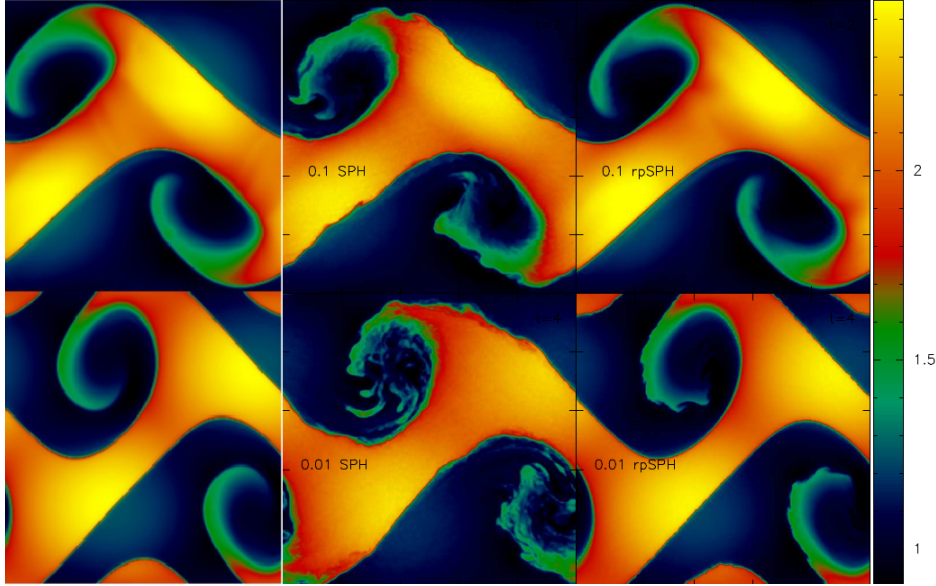
Figure 2.2: Late stage density distribution in a 2D Kelvin-Helmholtz test for a grid based code (left), SPH (right) and rpSPH (right). The initial velocity perturbation for the two fluids with different temperature and density is $0.1c_s$ in the top row and $0.01c_s$ in the bottom row. The rpSPH result is less noisy than SPH. (TA10)

f_i and f_j terms which, including effects that originate from varying smoothing length, assure entropy conservation in the Gadget-2 code by Springel and Hernquist. After applying few changes in the code the rpSPH version of WK04 SPH has this equation of motion

$$\frac{d\vec{v_i}}{dt} = \sum_{j=1}^{N} \frac{m_j}{2}[(\frac{P_j - P_i}{\rho_j^2} + \Pi_{ab})[\nabla_i W_{ij}(h_i) + \nabla_i W_{ij}(h_j)]]. \tag{2.18}$$

2.3 Stellar Potential and Other Parameters

The analytic expressions used to model a spiral galaxy are provided by Sanders(1977) and Wada and Habe(1992). The galactic Bulge, disk and

dark matter halo are represented by an axisymmetric potential given by

$$\Phi(R) = av(\frac{27}{4})^{1/2})(R^2 + a^2)^{-1/2} \tag{2.19}$$

where a is the core radius in kpc and v is the rotation velocity. The spiral arms of the galaxy are modeled with a non-axisymmetric potential defined as

$$\Phi(R, \phi) = \epsilon_0 \frac{aR^2\Phi(R)}{(R^2 + a^2)^{3/2}} Cos[2\phi + 2cot(i)ln(\frac{R}{R_0})] \tag{2.20}$$

with an arbitrary constant $R_0 = 0.9$ and the pitch angle i. ϵ_0 is a constant which defines how strong the non-axisymmetric potential is relative to the symmetric potential. The total galactic potential is calculated by a linear combination of the axisymmetric, eq. (2.19) and non-axisymmetric part, eq. (2.20).

$$\Phi_{ext} = \Phi(R) + \Phi(R, \phi) \tag{2.21}$$

A set of standard parameters adopted in all simulations carried out, if not explicitly stated otherwise. The core radius is $a = 1.0$ kpc. The flat rotation curve provided by the potential has a maximum rotation velocity of $v_{max} = 220km/s$. The galaxy has two spiral arms with a pitch angle of $i = 10^o$. Furthermore the potential strength is 10% of the symmetric potential ($\epsilon_0 = 0.10$). The pattern speed adopted is $\Omega = 26.1$ km/s. The parameters for the artificial viscosity are $\alpha = 1.0$ and $\beta = 2.0$.

The initial conditions are set by randomly placing N particles in a two dimensional disk of radius $r_{init} = 3.0$ kpc. These particles rest in a frame that is rotated with the constant pattern speed of the non axisymmetric potential. The resolution in most simulations is N = 50 000 particles. The smoothing length is allowed to vary with the constrain, that the amount of neighbor particles stays in between $N = 22$ and $N = 42$ and the average is kept constant at $N_{av} = 32$.

Chapter 3

Results

To investigate what causes the the wiggle instabilities seen in numerical simulations (WK04; DB06; KO02), the impact of varying gas temperature, spiral arm potentials and numerical resolution on the interarm structure in SPH and rpSPH is studied. The changes in the interarm structure at varying parameters are compared to predictions by the the K-H instability model and the clump shearing model. This includes a discussion of the behavior of the velocity gradient at different parameters. Further possible models, such as the magneto-Jeans instability are not discussed.

In particular, the gas temperature and the spiral arm potential strength are varied. It is then discussed, how and why the resolution should effect the interarm structure according to the clump shearing model.

Whether the interarm features seen in SPH and rpSPH are similar to observations is briefly discussed in a comparison to results by LV06. This is important to ensure the connection between the effects observed in numerical simulations and real galaxies. A general comparison of SPH and rpSPH is prefixed to detailed simulations.

3.1 General Pattern

SPH simulations show interarm substructures similar to observed extinction features. Parameter variations in the following sections will show that these features are relatively robust to potential and temperature variations in reasonable ranges. Figure 3.1 gives an example of a SPH simulation at a
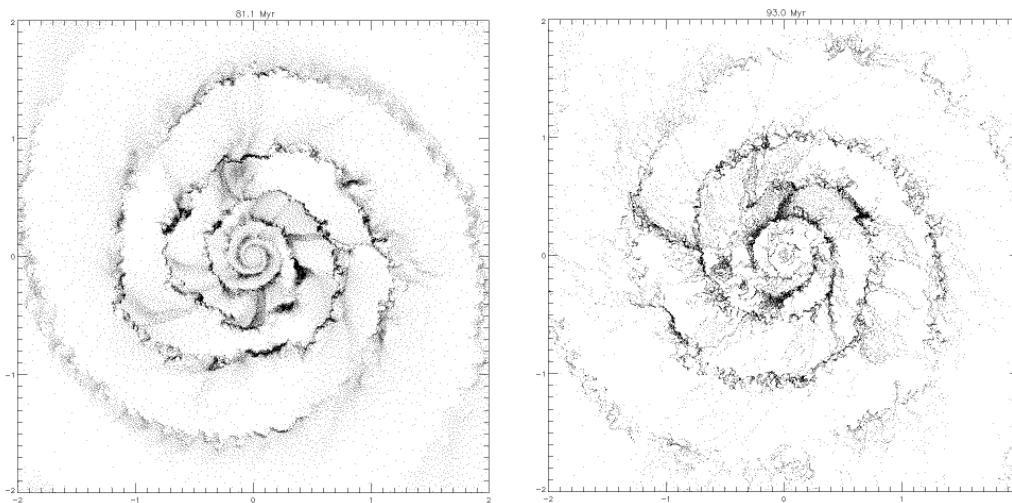
Figure 3.1: SPH (left) and rpSPH (right) simulations using a potential ratio of 10% and gas temperature of T = 25 000 K give an example for interarm structure seen at various parameter settings. The simulation time for the SPH snapshot is 81.1 Myrs and 93.0 Myrs for rpSPH.

potential ratio of 10% and a gas temperature of T = 25000 K that exhibits the filamentary structures, similar to feathers. Along the spiral arm potential a gas layer accumulates that shows wiggles with areas of higher and lower densities. The gas lanes extending from the spiral arms are usually associated with denser regions or clumps in the spiral arm. The pitch angles at which these spurs extend from the spiral arm are usually high, in most cases $40^o - 60^o$. The pitch angle decreases with distance to the spiral arm. While some are bent rather sharply, most spurs show slight angle decline.

SPH vs rpSPH

The relative pressure version of SPH changes the way pressure forces are implemented in SPH and is expected to reduce artificial velocity noise and to better resolve Kelvin-Helmholtz instabilities. Significant changes in the interarm structure are possible.

In fact the results of the rpSPH code did not differ greatly from SPH as can be seen in fig. 3.1. The fact that particles do not push each other apart anymore, which causes artificial background noise, leads to a greater density contrast. Even at high temperature and low potentials gas, which is smooth in SPH, shows voids and denser regions. Spurs appear thinner. Despite these changes, temperature and potential variations evaluated in the following sections show little difference between SPH and rpSPH in the behavior at various temperatures, potentials and resolutions. That rpSPH is able to resolve Kelvin-Helmholtz instabilities better does not seem to effect the interarm structure much.

Initial Condition Artifact

At early simulation times the interarm structure seen is biased by an initial condition artifact. The initially homogeneously distributed gas is accelerated towards the spiral potential and decelerated after spiral arm passage. This causes two over dense lines that clash into each other and cause at the spiral arm and spurs at 5-20 Myrs. This artificial effect is visible even at very high temperatures and should not be confused with structures due to K-H instabilities or the shearing of clumps. To avoid distortion caused by initial conditions or angular momentum loss, snapshots at a later stage t = 75 Myrs, corresponding to $\sim$1/3 of the total simulation time, were chosen as representations.
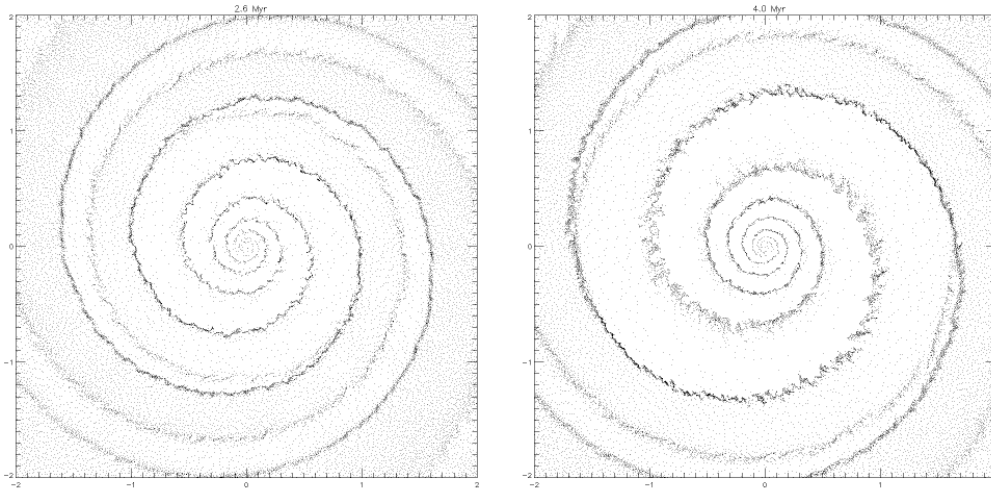
Figure 3.2: Early stages of a high temperature (T = 50000 K) and strong potential (ϵ_0=0.35) simulation showing two colliding dense gas lanes caused by the initial conditions.

3.2   Dependence on Temperature

Both theoretical models, clump shearing and K-H instability, predict a structure decrease at higher gas temperatures. Dobbs observed an interarm structure decrease in DB06. As described in 1.2.2 she attributes this to weaker shocks and smoother interarm gas due to higher gas temperature and therefore pressure. In the WK04 model a temperature raise is also expected to suppress K-H instabilities. Higher temperatures cause weaker shocks, which goes along with a decrease in the $v_{parallel}$ gradient across spiral shocks. Smaller velocity gradients lower the denominator in equation 1.4, thus, necessary conditions for K-H stability are fulfilled more easily.

Simulations covering a temperature range from 50 K to 300 000 K with SPH and rpSPH at standard settings confirmed the expected interarm structure decrease at higher temperatures. 3.3 and 3.4 show the steady decline in structure between T = 50 000 K and T = 75 000 K in SPH and rpSPH simulations. It is now of interest, to explore when the temperature reaches
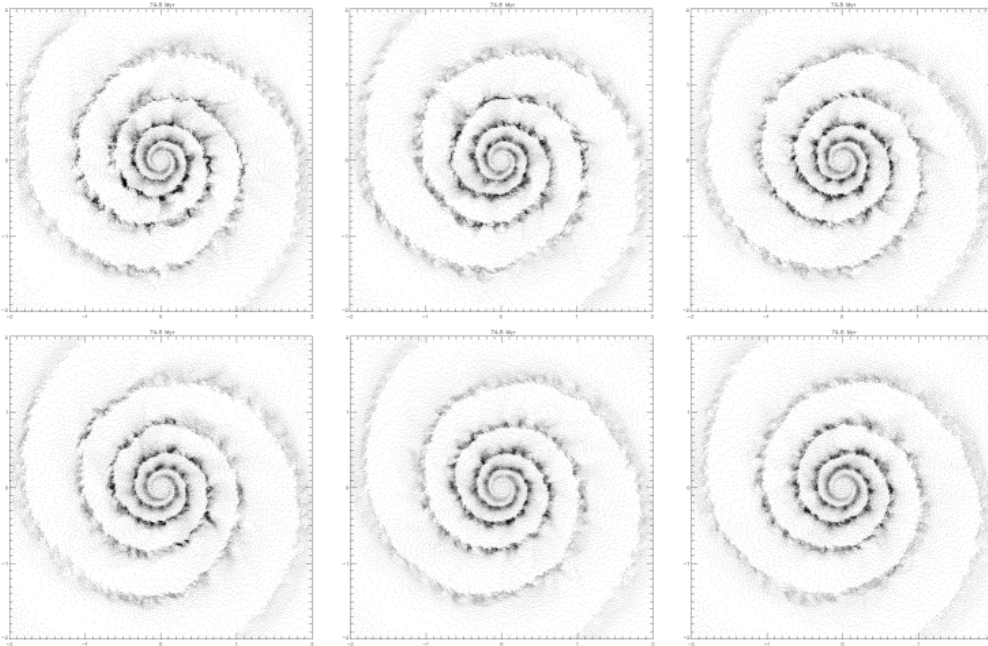
Figure 3.3: Shown are snapshots at t=74.8 Myrs for SPH simulations covering a temperature range of T = 50 000 K (top left) to 75 000 k (bottom right) in 5 000 K steps. While at the high temperature of T = 50 000 K minimal interarm structure is still visible, at T = 75 000 K the interarm region is smooth, which therefore is the transition temperature.

a point, where interarm structure , especially feathering, disappears. In the following, this temperature will be called *transition temperature*, which is defined as the temperature, where interarm structure such as feathers disappear. If the temperature is set to the transition temperature the dependence of feather morphology appearance on other parameters should become more significant. Unfortunately this transition is not sudden.

For standard parameters the transition temperature is found to be $T_{trans} \approx$ 75000 K. See fig. 3.3 and 3.4. To ensure comparability to simulations in WK04 a potential ratio of 10% is adopted.
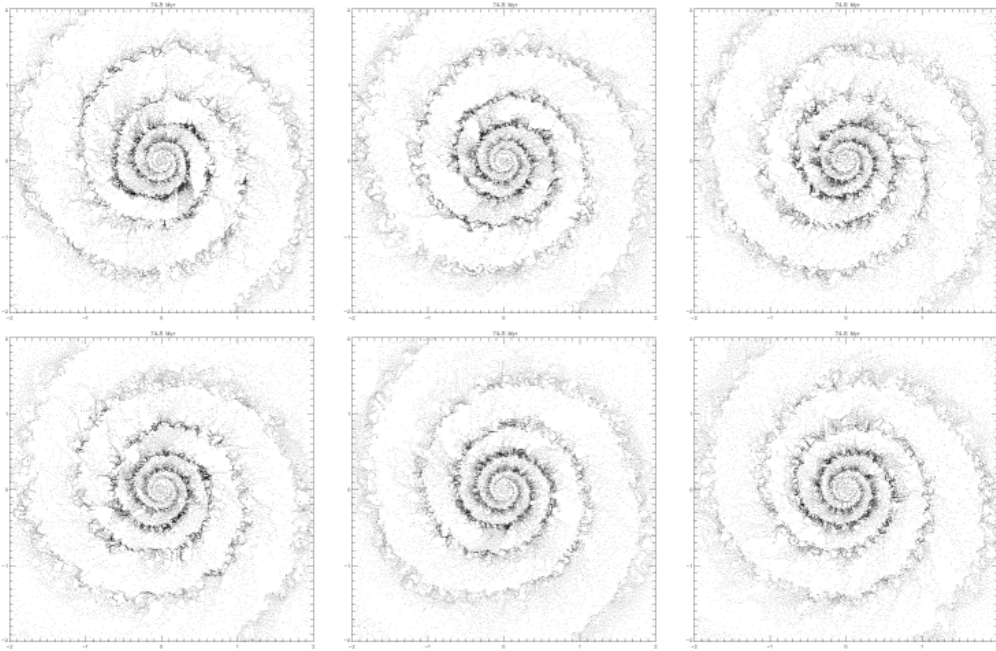
Figure 3.4: Shown are snapshots at t=74.8 Myrs for SPH simulations covering a temperature range of T = 50 000 K (top left) to 75 000 K (bottom right) in 5 000 K steps. While at the high temperature of T = 50 000 K minimal interarm structure is still visible, at T = 75 000 K the interarm region is smooth, which therefore is the transition temperature.

Velocity Gradient Dependence on Temperature

To further evaluate how the spiral arm potential strength decreases the shear velocity according to the K-H instability model, I plotted the velocity gradient across the shock region for SPH and rpSPH simulations at varying temperature. To achieve this goal, the minimum of the non-axisymmetric potential has been calculated and approximated by three lines. Furthermore, the velocity is projection onto these lines and plotted against the distance to the approximated potential for a certain area. A rectangular cutout of (0.4 x 0.8) kpc is marked as red box in following figures.

37

Figure 3.5: The top row shows snapshots of SPH simulations with a fixed potential ratio of $\epsilon_0 = 0.1$ using different gas temperatures T = 10000 K (a) ,T = 75000 K (b) and T = 120000 K (c). The white lines mark the spiral arm potential minima. The bottom row shows the velocity projection onto the spiral potential against the distance to the potential minimum for all particles in an area indicated with a red box for each different snapshot. The plots show a subsequent velocity gradient decrease at higher temperatures.

I found a subsequent decrease in the velocity gradient in SPH and rpSPH simulations using a fixed potential covering a gas temperature range from T = 10 000 K up to T = 120 000 K. The velocity projection plots for SPH, fig. 3.5, and rpSPH, fig. 3.6 show snapshots for some temperature values. A closer examination of figures 3.9, 3.10, 3.5 and 3.6 reveals, that not exactly the same point in time is used to compare all simulations. The snapshots with the best visibility have been chosen within a range of 5 Myrs. This

is justified by the fact, that although the slope visibility is limited in single snapshots, in all cases the slope is visible in a movie resolving the 180 Myrs time evolution in 270 images.
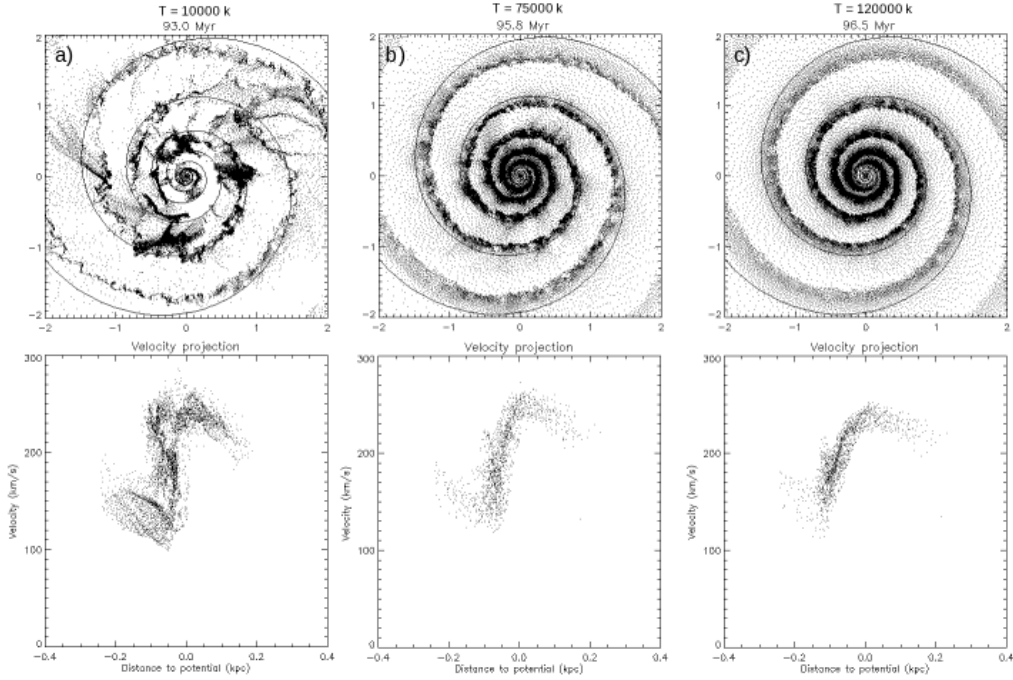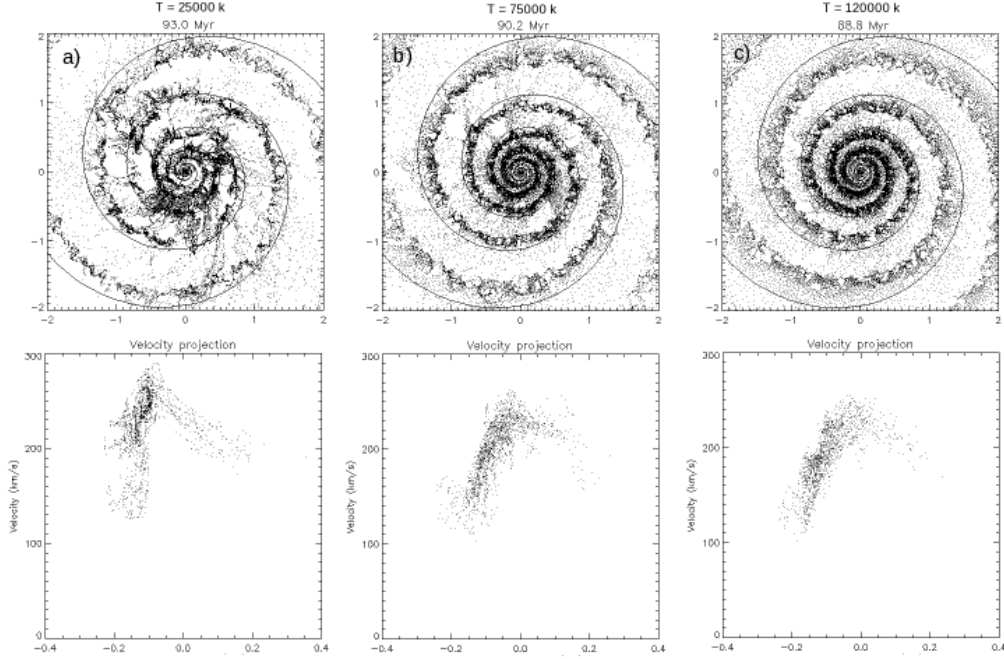

Figure 3.6: The top row shows snapshots of rpSPH simulations with a fixed potential ratio of $\epsilon_0 = 0.1$ using different gas temperatures T = 10000 K (a) ,T = 75000 K (b) and T = 120000 K (c). The white lines mark the spiral arm potential minima. The bottom row shows the velocity projection onto the spiral potential against the distance to the potential minimum for all particles in an area indicated with a red box for each different snapshot. The plots show a subsequent velocity gradient decrease at higher temperatures.

3.3 Dependence on Spiral Potential Strength

Another important parameter for which both models make predictions is the ratio of non-axisymmetric and axisymmetric potential strength. In the clump shearing model, higher potentials and therefore stronger shocks are expected to increase the amount of interarm structure. A stronger spiral arm potential causes a higher acceleration and stronger compression of the gas in the shock region. This brings the gas particles from different orbits closer together and increases the angular momentum transfer between these, which leads to a closer grouping and more dense clumps. These then get sheared and form more feathers. Weaker shocks leave the particle velocities unchanged and less clumps and spurs are expected.

In the K-H instability model a higher velocity shear is expected to make the fluid layers more unstable. The stronger the non-axisymmetric part, the more prominent the spiral arms. Higher acceleration at the spiral arms results in stronger shocks and a larger velocity gradient perpendicular to the shock. At very low potentials and shears the wiggles are therefore expected to disappear. Starting at the potential-ratio adopted in WK04 is 10% I extended the scope of the simulations to lower ratios 2.5% , 5.0%, 7.5% and higher ratios 10%, 15% and 20%.

Potential variations were performed for multiple fixed temperatures ranging from T = 10000 K to T = 120000 K. One finding is, that higher spiral arm potentials increase the angular momentum loss of the gas. Another effect amplified at higher potentials (> 10 %), which compromises the first fifth of the simulation, is described in sec. 3.1.

Figure 3.7 and 3.8 show the outcome of simulations varying the potential ratio for SPH and rpSPH. The temperature T = 65000 K is set close to the transition temperature, so that the gain and loss of interarm structure is better visible.

Figure 3.7: SPH simulations at T = 65000 K with potential ratios ranging from 2.5% (a), 5.0% (b), 7.5% (c), 10.0% (d), 15.0%(e) and 20.0%(f) showing an increase in interarm structure at higher potentials.
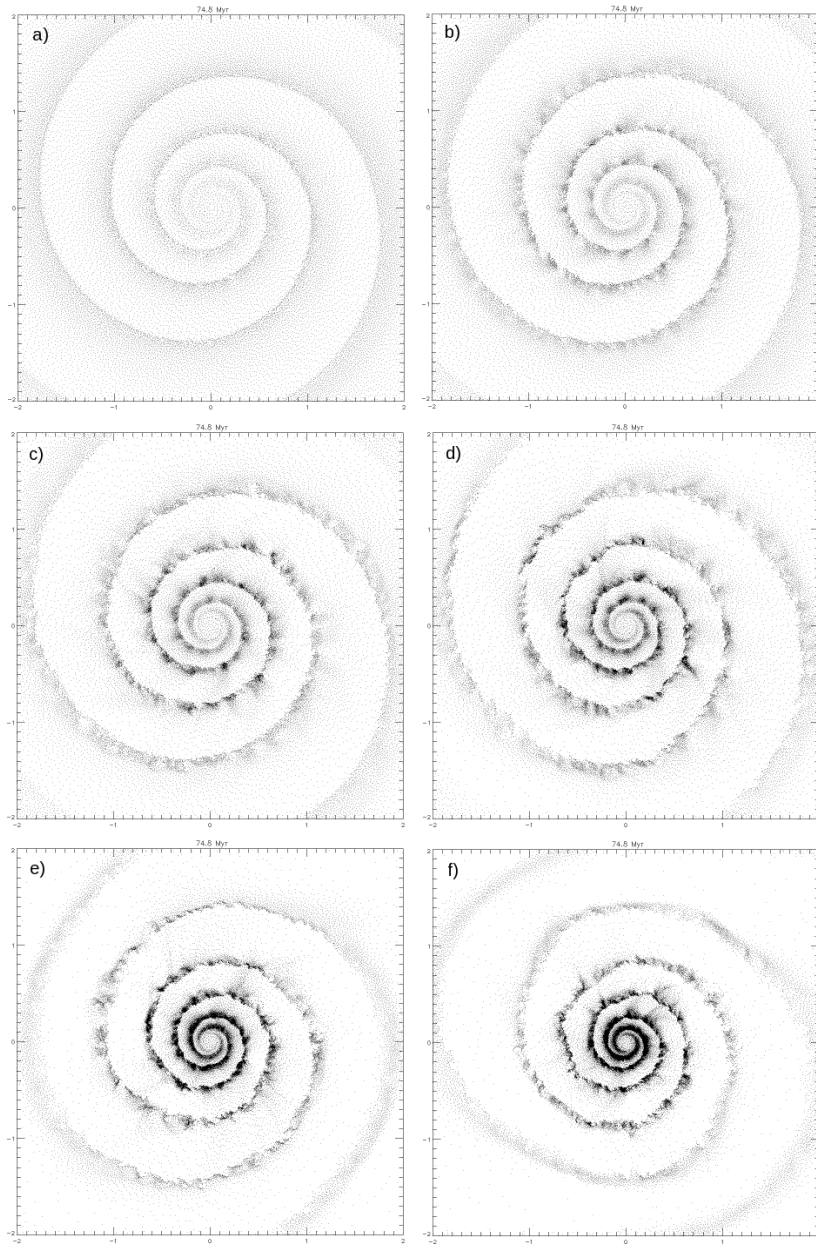
Figure 3.8: rpSPH simulations at T = 65000 K with potential ratios ranging from 2.5% (a), 5.0% (b), 7.5% (c), 10.0% (d), 15.0%(e) and 20.0%(f) showing an increase in interarm structure at higher potentials.
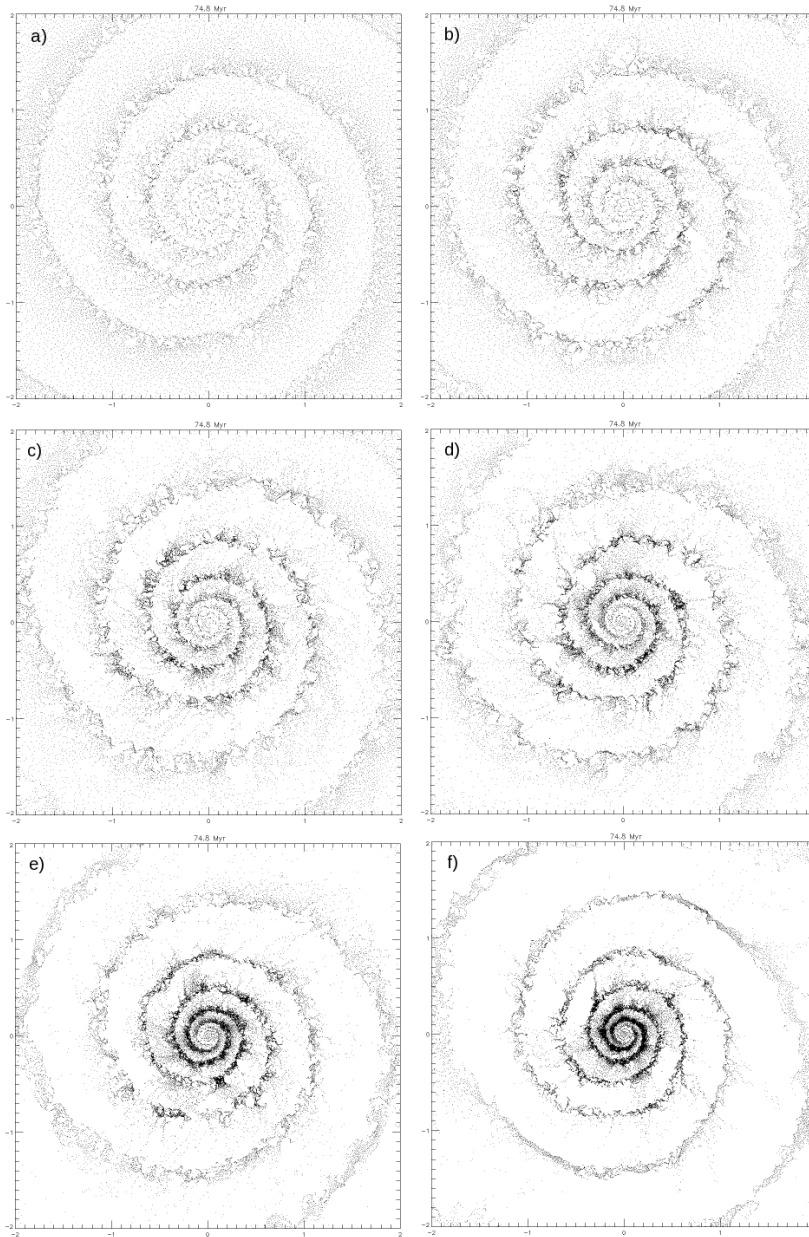
At low potentials (2.5%) there is little structure within the arms and none in the interarm region. Similar to high temperature simulations interarm gas is present and homogeneously distributed. Below a potenital ratio of 10% an increase of potential strength increases the amount of interarm structure. At higher potentials (> 10%) there is less gas in the interarm region. The density in the spiral arms is higher and the gas shows more structure. In summary, spiral arm clumpyness and the amount of interarm features like feathers increases with increasing potential ratio up to a maximal appearance. Above this maximum, the amount of spurs decreases. This has two reasons. First, the spiral arm potential reaches unphysical values. It gets so strong, that the particles do not maintain their circular orbits around the center anymore and fall into the center. Second, according to equation (1.4) the Richardson number J is proportional to the density gradient across spiral arms. An increasing buoyancy force suppresses K-H instabilities. Since interarm structure depends on gas temperature as described in sec. 3.2, this maximum is also temperature dependent. For the temperature range of 50 000 K to 75 000 K the maximum appearance of interarm features occurs at a ratio of 10%. This finding is consistent with the predictions made by the K-H instability model and the clump model. A realistic potential increase is expected to raise the velocity shear and therefore increase the amount of wiggles and feathering. The increase in interarm structure at higher potentials and the decrease at lower potentials is also consistent with the clump shearing model. Additionally it is noticed, that the wiggle instability also occurred at a potential ratio of 2.5% and a sound speed of 7 km/s. KO06 found that the wiggle instability to disappear below the force ratio of 4% in non-magnetic, non-self-gravitating 2-D grid based simulations. Thus the result is inconsistent. SPH simulations show, that at low potentials structure can be found as long as the temperature is low.

Velocity Gradient Dependence on Spiral Arm Potentials

To further evaluate whether increasing spiral arm potentials really increase the velocity shear as expected by the K-H instability model, I plotted the velocity parallel to the spiral arms for SPH and rpSPH simulations with varying potential ratios. The plot is created as described in sec. 3.2. The velocity gradient has been evaluated for potential ratios ranging from 2.5% up to 20%.

Figure 3.9: The top row shows snapshots of SPH simulations at a fixed gas temperature of T = 65 000 K using different spiral arm potential strength of 5.0% (a) , 10.0% (b) and 15% (c). The white lines mark the spiral arm potential minima. The bottom row shows the velocity projection onto the spiral potential against the distance to the potential minimum for all particles in an area indicated with a red box for each different snapshot. The plots show a subsequent velocity gradient increase at higher potential strengths.

For both codes the velocity slope is found to increases in dv and dx with increasing potential strength. This is shown in several snapshots for SPH in fig. 3.9 and for rpSPH in fig. 3.10.
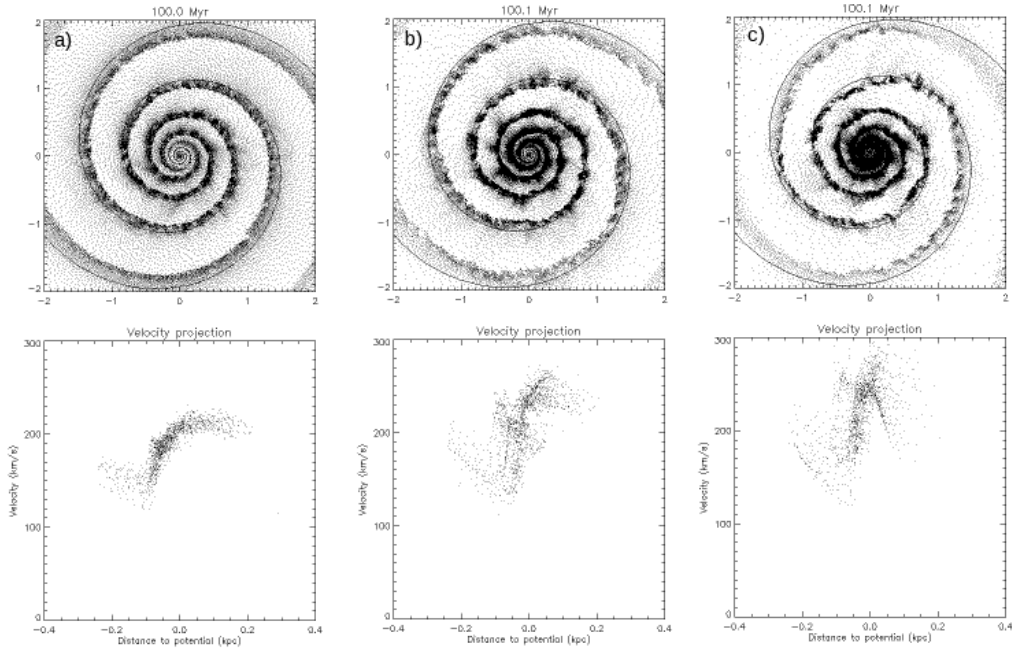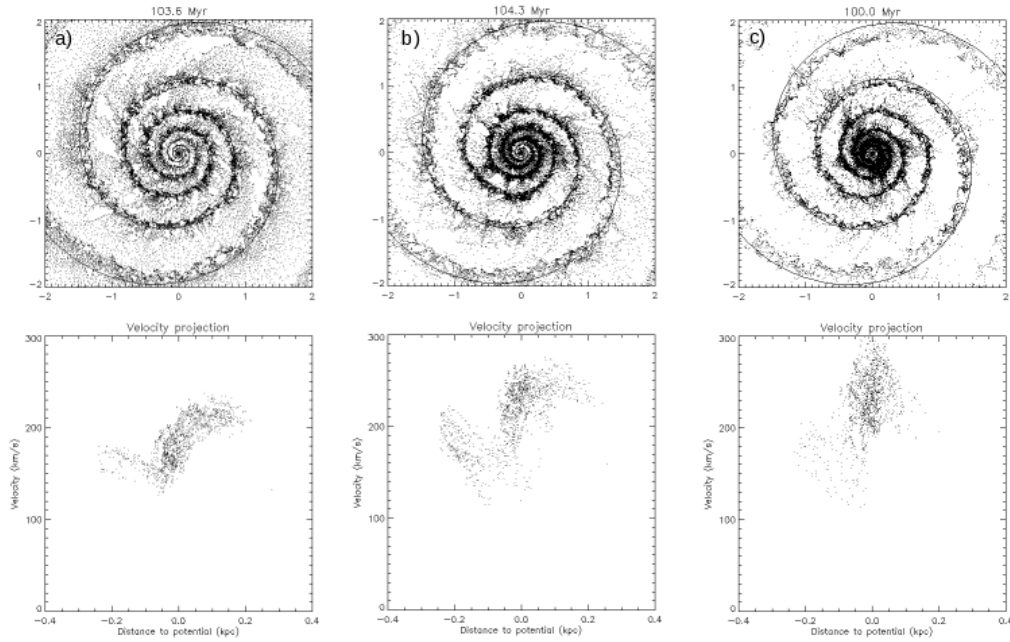

Figure 3.10: The top row shows snapshots of rpSPH simulations at a fixed gas temperature of T = 65 000 K using different spiral arm potential strength of 5.0% (a) , 10.0% (b) and 15% (c). The white lines mark the spiral arm potential minima. The bottom row shows the velocity projection onto the spiral potential against the distance to the potential minimum for all particles in an area indicated with a red box for each different snapshot. The plots show a subsequent velocity gradient increase at higher potential strengths.

3.4 Total Angular Momentum in SPH and rpSPH

In both codes, SPH and rpSPH, the total angular momentum is not conserved and decreases over time. The reason is, that neither neither my SPH or rpSPH implementation models the reaction of the gas mass on the analytical stellar potential. The angular momentum of the gas is transferred to the stellar potential.
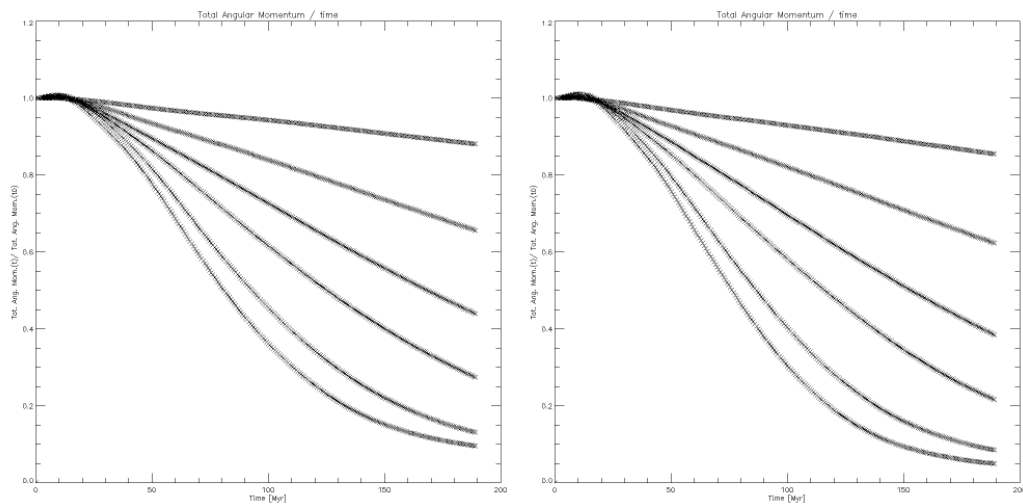
Figure 3.11: Total angular momentum as a function of time for SPH (left) and rpSPH (right) at a fixed temperature of T = 65000 K and potential ratios varying from 2.5%, 5.0%, 7.5%, 10.0%, 15% and 20% showing a strong spiral arm potential dependence with high losses at higher spiral arm potentials.

As described in sec. 2.2 the angular momentum is not conserved in rpSPH due to the non-symmetric implementation of pressure forces. It has to be investigated, whether this compromises the simulation results of rpSPH and SPH. Figure 3.11 shows the total angular momentum as a function of time for the SPH and rpSPH simulations shown in 3.7 and 3.8. After a short plateau the total angular momentum decreases linearly. While at a potential ratio

of 2.5% the total angular momentum loss after two rotational periods(180 Myrs) is $\approx$ 10%, at a ratio of 10% the loss sums up to $\approx$ 70%. At 15% and 20% the loss saturates, because high densities and therefore pressures at the center of the galaxy prevent more gas from in falling. Later stages of the simulations, especially at higher spiral arm potentials should not be used to identify interarm structure to ensure realistic conditions. In most cases I use snapshots at $\sim$90 Myrs, which is half of the total simulation time, for comparison.

rpSPH shows a slightly higher angular momentum loss than SPH. This may be accounted to changes in the momentum equation. But the effect is negligible compared to the angular momentum loss caused by the spiral arm potential. As seen in 3.12 varying the gas temperature changes the angular momentum only slightly in SPH and rpSPH.

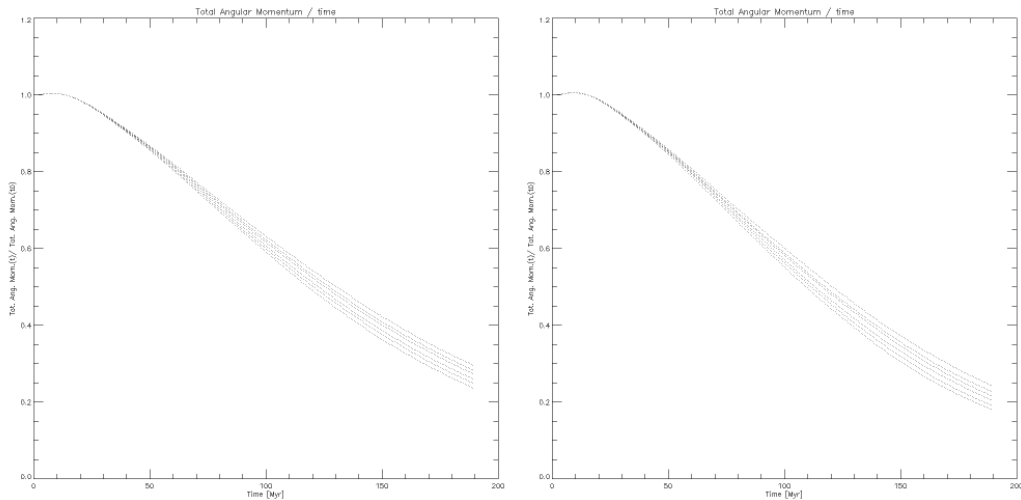

Figure 3.12: The Total angular momentum as a function of time in SPH (left) and rpSPH (right) simulations at a fixed spiral arm potential of $\epsilon_0 = 0.1$ and varying temperatures shows little temperature dependence. The temperature range is T = 50000 K to 75 000 K.

47

3.5 Dependence on Resolution

So far temperature and potential variations back the clump shearing and the Kelvin-Helmholtz instability models. To distinguish both models one needs to find a parameter that is expected to change the interarm structure in one model, but not the other.

In the clump shearing model the amount of interarm structure is depending on the clumpyness of the interarm region. One possibility now is to change the clumpyness in the interarm region artificially. At a low resolution the sampling of the density distribution is less good which leads to a higher density noise. This results in regions with higher density which can be seen as artificial clumps. In this case an increase in the amount of feathers is expected with decreasing resolution, because of the increase of random density noise.

DB06 performed SPH simulations with 1×10^6 and 4×10^6 particles, see sec. 1.2.2. While simulations with a directly comparable resolution to DB06 were beyond our hardware capabilities, it could be tested whether the amount of structure varies with the number of particles at lower resolutions. To increase the visibility of interarm structure changes, the resolution variations are carried out around the transition temperature. Furthermore the amount of particles used in SPH simulations is an important parameter for the quality of the simulation outcome. A low resolution leads to a poor structure visibility and can cause numerical artifacts.

Fewer particles, result in a larger smoothing length, smoothing out changes in physical quantities varying within $r < 2h$. This especially effects discontinuities. Assuming a high velocity gradient and a pressure discontinuity at the shock regions of spiral arms, resolution effects could influence the simulation outcome.

SPH simulations were carried out covering a range of 10 000 particles to 100 000 particles for gas temperatures of T = 30000 K up to T = 120000 K. rpSPH simulations cover a temperature range of T = 50000 K to T = 120000 K. Figure 3.13 shows the simulation outcome for temperatures close to the

Figure 3.13: SPH simulation snapshot at t=74.8 Myrs assuming gas temperatures of T = 65000 K and potential strength of $\epsilon_0 = 0.1$ with 25 k (top left), 50 k (top right), 75 k (bottom left) and 100 k (bottom right) particles.

transition temperature. It appears as the amount of interarm structure increases with resolution. This can be accounted to a higher visibility of density contrast, although the feather spacing stays roughly constant and the dense clumps in the spiral arm are also present at lower resolutions. Therefore, the amount of feathers does not change significantly. A simulation with the
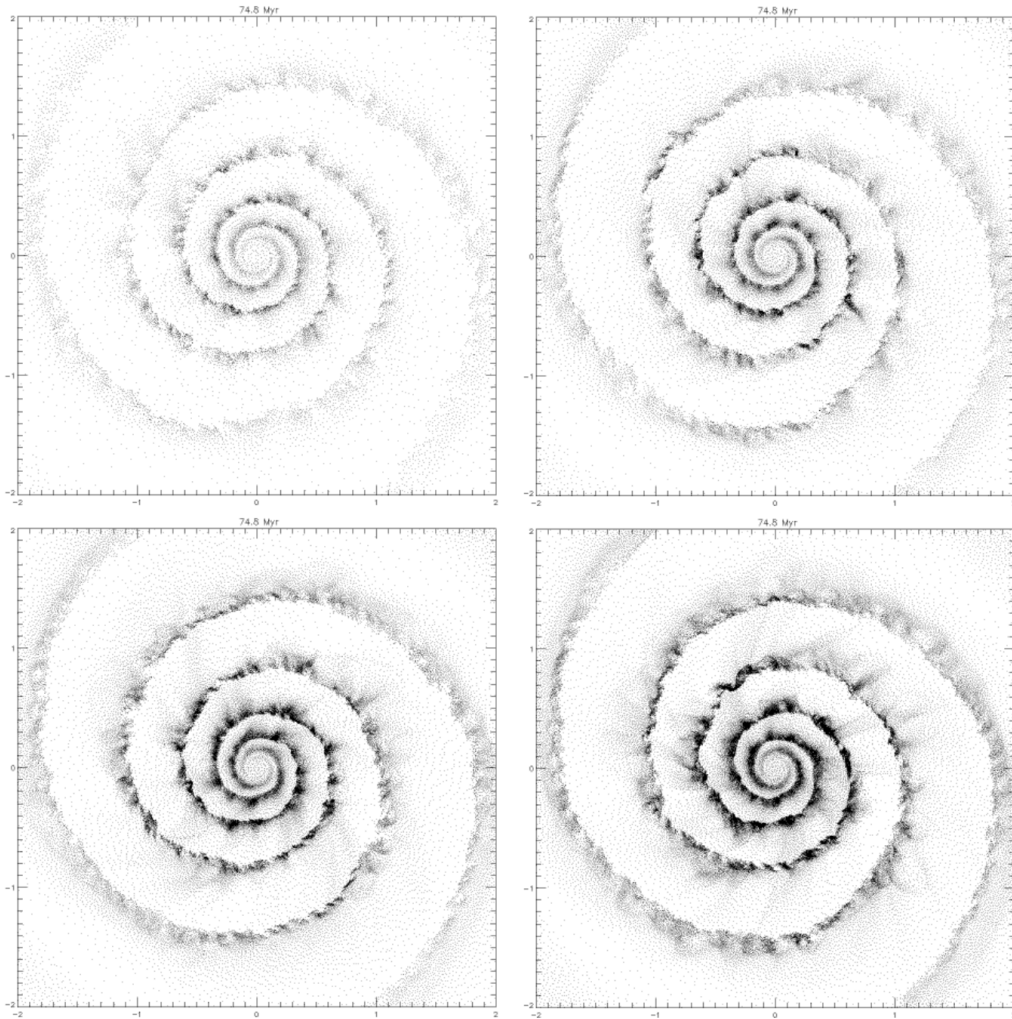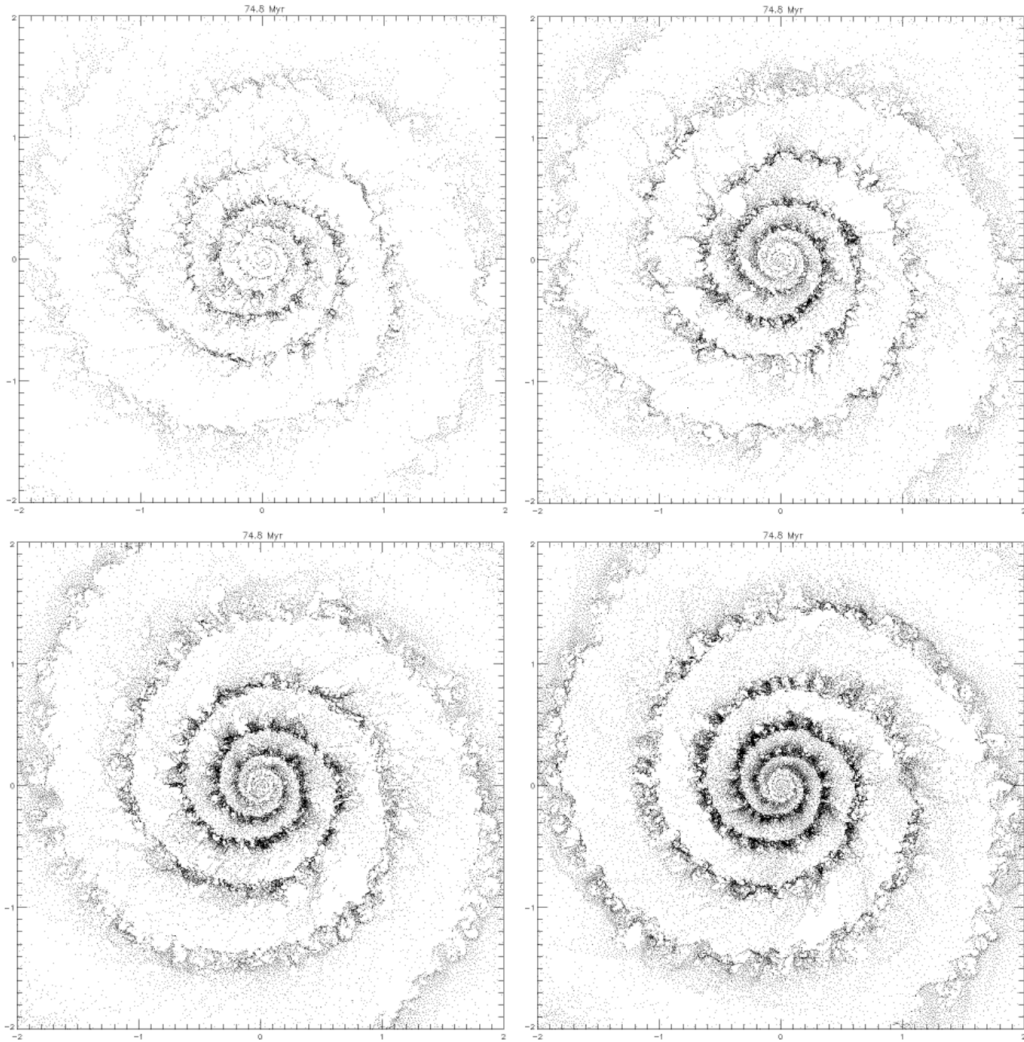
Figure 3.14: rpSPH simulation snapshot at t=74.8 Myrs assuming gas temperatures of T = 65000 K and a potential ratio of $\epsilon_0 = 0.1$ with 25 k (top left), 50 k (top right), 75 k (bottom left) and 100 k (bottom right) particles.

same parameters using rpSPH is shown in fig. 3.14. The rpSPH simulations generally show more small scale structures in spiral arms. While the amount of small scale structure in the spiral arm increases due to a better visibility, hardly any changes in the interarm regions

In conclusion, either artificial clumping is not a dominant effect at resolutions of 75000 and 100000 at this particular setting or it is present with a roughly constant effect that only changes at much higher resolutions. The fact that the anticipated increase of feathering at lower resolution was not found, is opposing to the expectations based on the clump shearing model of DB06.

3.6   Comparison with Observation

The features we found in our simulations largely resemble observed feathers. Since it is only meaningful to investigate the cause of the wiggle instability if it is related to feathers in spiral galaxies, whether the interarm structures created are similar to recent observations, has to be thoroughly examined. To do that, one has to look at the characteristics of feathers and in which galaxies feathering occurs.

According to fig. 1.4 feathers are found in only a few early type spirals, Sa and Sab. Early type galaxies are characterized by more tightly wound spirals. WK04 finds the wiggle instability suppressed in tightly wound spirals. Additionally , according to eq. 1.5 Kelvin-Helmholtz stability increases with increasing pitch angle. No feathers were found in later Hubble types Sc and Scd. Late type spirals exhibit loosely wound spirals, but are also characterized as very faint with ragged and less well ordered spiral arms [direct quote from book]. Low luminosities and ragged spiral arms indicate weak spiral arm potentials. Weak spiral potentials cause weak spiral shocks, which do not create a sufficient strong velocity shear for K-H instabilities or the clump shearing to occur, as further outlined in sec. 3.3.

The spurs produced in SPH simulations as seen in fig. 3.15 are trailing features. They extend at high pitch angles of $(40^o - 60^o)$, which matches the observed feather pitch angles of $\sim 50^o$ in earlier surveys (LY70; LV06). The pitch angle of spurs is found to decrease with increasing distance to the spiral arms due to shearing in both, SPH simulations and LV06.
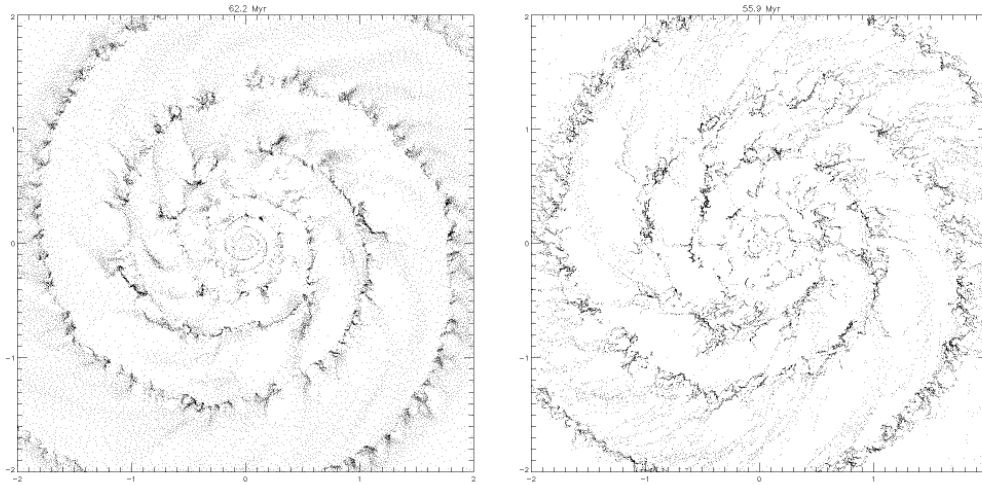
Figure 3.15: SPH (left) and rpSPH (right) simulations with a potential ratio of 2.5% and gas temperature of T = 5000 K corresponding to a sound speed of 7 km/s showing regular interarm structure.

Moreover they commonly originate from overdense regions in the spiral arm. This is consistent with findings by LV06, that junctions between feathers and spiral arms associate in "nearly 100%"(LV06) with dense clumps in CO(1-0) emission maps, as seen in fig. 3.1. A change in the curvature of spurs from leading to trailing along the spiral arm, as noticed by La Vigne et al., was not found in our simulations, independent from parameter variations.

Fig. 3.15 shows simulations witch a moderate potential ratio of 5% and a sound speed of $c_s = 7$ km/s, which is the same gas temperature adopted for NGC 5194 and NGC 0628 (LV06). The spacing between spurs is found to be $\approx 200 - 300pc$, roughly matching NGC 0628 and NGC 5194 where 46 out of 65 feathers show spacings in the range of (100 - 400) pc, (see fig. 1.7). Although, simulations could reproduce this particular case, feather spacing might be sensitive to spiral galaxy parameters such as the spiral arm potential strengths. A detailed comparison requires feather spacings for several

galaxies covering a range of potential strength.

Our simulation reproduces most observed features such as feather shape, pitch angles and association with dense clumps, as characterized by La Vigne et al.

Chapter 4

Conclusion

The comparison of SPH and rpSPH simulations of spiral galaxy substructure with the LV06 HST survey and earlier observations ensured, that the wiggle instability found produces similar interarm structure as observed in various spiral galaxies. Both codes are capable of producing spurs extending from the spiral arms at high pitch angles of $40^o - 60^o$, showing a pitch angle decrease with increasing distance to the spiral arm. Spurs in SPH simulations form from overdense regions on the spiral arm, similar to observations with CO(1-0) maps. Furthermore feather spacings of the order (200-300) pc were found at comparable settings to KO06.

The main question addressed is whether parameter variations affect the wiggle instabilities as expected by K-H instabilities and the clump shearing model. Simulations covering a wide temperature range found a decrease in the amount of interarm structure at higher temperatures. Changes in the non-axisymmetric/axisymmetric potential ratio between 2.5% and 20% found an increase of interarm structure up to a critical value, where it then decreases. The point where no spurs on the interarm are found shifts to higher potentials at higher temperatures and to lower potentials at lower temperatures. Correspondingly, the velocity gradient across spiral arms is found to increase with a higher potential ratio and a lower temperature.

This behavior follows the predictions that can be made from the Richardson number criteria. It is also consistent to the clump shearing model of Dobbs and Bonnell. Higher temperature smooths the pre-shock gas out so there are no clumps to get sheared and lower potential ratios cause weaker shocks with less influence on the angular moment.

While temperature and potential variations could not differentiate between the models, resolution variations were used to test distinguish between both models. Lowering the resolution makes the interarm region artficially clumpy, which is expected to cause more feathering in the clump shearing model. The amount of feathering was found to be independent from resolution.

This work sees some evidence, that wiggle instabilities and interarm structure found in SPH and rpSPH behave consistently with predictions made by K-H Instabilites and somewhat disfavors the clump instability model.

Future Research

To further consolidate the conclusion that increasing resolution does not change the number of observed feathers a method more independent from personal judgement should be realized. For example, one could calculate surface density instead of using the SPH particle distribution and quantify the contrast.

Moreover, it should be tested if the resolution has similiarly little effect in simulations including more realistic conditions, e.g. self-gravity. Additionally three dimensional simulations should be performed to falsify, whether the observed wiggle instability is a numerical artifact of a two dimensional disk.

Bibliography

[1] [SA61] Sandage, A.; The Hubble atlas of galaxies, Washington: Carnegie Institution, 1961

[2] [WE70] Weaver, H. F.; Some Characteristics of Interstellar Gas in the Galaxy, IAU Symp. 39, Interstellar Gas Dynamics, 22

[3] [LY70] Lynds, B. T.; The Distribution of Dark Nebulae in Late-Type Spirals , IAU Symp. 38, The Spiral Structure of Our Galaxy, 26

[4] [PD73] Piddington, J. H.; The Density-Wave Theory of Galactic Spirals, Astrophysical Journal, vol. 179, 1973, pp. 755-770

[5] [SL66] Lin, C.C., Shu F.H.; On the Spiral Structure of Disk Galaxies, II. Outline of a Theory of Density Waves, Proceedings of the National Academy of Sciences, Volume 55, 1966, pp. 229-234

[6] [EL80] Elmegreen, D.M.; An optical analysis of dust complexes in spiral galaxies, Astrophysical Journal Supplement Series, vol. 43, 1980, p. 37-56

[7] [DB06] Dobbs, C.L., Bonnell I.A.; Spurs and feathering in spiral galaxies, Monthly Notices of the Royal Astronomical Society, col. 367, 2006, pp. 873-878;

[8] [LV06] La Vigne, M.A., Vogel, S.N. Ostriker, E.C.; A Hubble Space Telescope Archival Survey of Feathers in Spiral Galaxies, The Astrophysical Journal, vol. 650, 2006, pp. 818-834

[9] [WK04] Wada, K., Koda, J.; Instabilities of spiral shocks - I. Onset of wiggle instability and its mechanism, Monthly Notices of the Royal Astronomical Society, vol. 349, 2004, pp. 270-280;

[10] [BB88] Balbus, S.A.; Local interstellar gasdynamical stability and substructure in spiral arms, Astrophysical Journal, vol. 324, 1988, p. 60-74

[11] [KO01] Kim, W.T., Ostriker, E.C.; Growth of Self-Gravitating Structures in Models of Magnetized Galactic Gas Disks, The Astrophysical Journal, vol. 559, 2001, pp. 70-95

[12] [KO02] Kim, W.T., Ostriker, E.C.; Formation and Fragmentation of Gaseous Spurs in Spiral Galaxies, The Astrophysical Journal, vol. 570, 2002, pp. 132-151

[13] [KO06] Kim, W.T., Ostriker, E.C.; Formation of Spiral-Arm Spurs and Bound Clouds in Vertically Stratified Galactic Gas Disks, The Astrophysical Journal, vol. 646, 2006, pp. 213-231

[14] [SC01] Scoville, N.Z. et al.; High-Mass, OB Star Formation in M51: Hubble Space Telescope H and Pa Imaging, The Astronomical Journal, vol. 122, 2001, pp. 3017-3045

[15] [KE03] Kennicutt, R.C. et al.; SINGS: The SIRTF Nearby Galaxies Survey, Astronomical Society of the Pacific, vol. 115, 2003, pp. 928-952

[16] [RH01] Regan, M.W. et al.; The BIMA Survey of Nearby Galaxies I, The Astrophysical Journal, vol. 561, 2001, pp. 218-237

[17] [RH03] Helfer, T.T.; The BIMA Survey of Nearby Galaxies II, The Astrophysical Journal Supplement Series, vol. 145, 2003, pp. 259-327

[18] [ST88] Strong, A.W. et al.; The radial distribution of galactic gamma rays IV, Astronomy and Astrophysics , vol. 207, 1988, p. 1-15

[19] [SK84] Shostak, G.S., van der Kruit P.C.; Studies of nearly face-on spiral galaxies. II, Astronomy and Astrophysics, vol. 132, 1984, p. 20-32

[20] [SE84] Sellgren, K.; The near-infrared continuum emission of visual reflection nebulae, Astrophysical Journal, vol. 277, 1984, p. 623-633

[21] [CA05] Calzetti, D. et al.; Star Formation in NGC 5194 (M51a): The Panchromatic View from GALEX to Spitzer, The Astrophysical Journal, vol. 633, 2005, pp. 871-893

[22] [SN92] Stone, J.M, Norman, M.L.; ZEUS-2D: A radiation magnetohydrodynamics code for astrophysical flows in two space dimensions I, Astrophysical Journal , vol. 80, 1992, p. 753-790

[23] [BE90] Benz, W.; The Numerical Modeling of Nonlinear Stellar Pulsations, Kluwer Academic Publishers, Dordrecht, 1990, p. 269

[24] [MO92] Monaghan, J.J.; Smoothed particle hydrodynamics, Annual review of astronomy and astrophysics, vol. 30 ,1992, p. 543-574

[25] [CO81] Caldwell, J.A.R., Ostriker J.P.; The mass distribution within our Galaxy - A three component model, Astrophysical Journal, vol. 251, 1981, p. 61-87

[26] [BT87] Binney, J., Tremaine, S.; Galactic dynamics, Princeton, NJ, Princeton University Press, 1987, p. 747

[27] [CG02] Cox, D.P., Gomez, C.; Analytical Expressions for Spiral Arm Gravitational Potential and Density, The Astrophysical Journal Supplement Series, vol. 142, 2002, pp. 261-267

[28] [EL02] Elmegreen, D.M., Star Formation from Galaxies to Globules, The Astrophysical Journal, vol. 577, 2002, pp. 206-220

[29] [LS93] Liou, M.S., Steffen, C.J.; A New Flux Splitting Scheme, Journal of Computational Physics, vol. 107, 1993, p. 23-39

[30] [YA91] Yabe, T., Aoki T.; A universal solver for hyperbolic equations by cubic-polynomial interpolation I, Computer Physics Communications, vol. 66, 1991, p. 219-232

[31] [NM77] Nelson, A.H., Matsuda, T.; On one-dimensional galactic spiral shocks, R. Astron. Soc., vol. 179, 1977, p. 663-670

[32] [TA10] Abel T.; rpSPH: a much improved Smoothed particle Hydrodynamics Algorithm, arXiv:1003.0937, 2010

[33] [CH61] Chandrasekhar, S.; Hydrodynamic and Hydromagnetic Stability, Dover, New York, 1961, p. 481

[34] [SH02] Sprignel, V., Hernquist, L.; Cosmological smoothed particle hydrodynamics simulations: the entropy equation, Mon. Not. of the R. Astron. Soc., vol. 333, 2002, pp. 649-664

[35] [BA95] Balsara, D.S.; von Neumann stability analysis of smooth particle hydrodynamics–suggestions for optimal algorithms, J. of Comp. Phy., vol. 121, 95, pp.357-372

[36] [WA08] Wada, K.; Instabilities of Spiral Shocks. II. A Quasi-Steady State in the Multiphase Inhomogeneous ISM, The Astrophysical Journal, vol. 675, 2008, pp. 188-193